

REPORT DOCUMENTATION PAGE			Form Approved OMB No. 0704-0188
<p>Public reporting burden for this collection of information is estimated to average 1 hour per response, including the time for reviewing instructions, searching existing data sources, gathering and maintaining the data needed, and completing and reviewing the collection of information. Send comments regarding this burden estimate or any other aspect of this collection of information, including suggestions for reducing this burden, to Washington Headquarters Services, Directorate for Information Operations and Reports, 1215 Jefferson Davis Highway, Suite 1204, Arlington, VA 22202-4302, and to the Office of Management and Budget, Paperwork Reduction Project (0704-0188), Washington, DC 20503.</p>			
1. AGENCY USE ONLY (Leave blank)	2. REPORT DATE	3. REPORT TYPE AND DATES COVERED	
	12/1/95	Final, Sept 91 - Sept 95	
4. TITLE AND SUBTITLE		5. FUNDING NUMBERS	
Experimental and Theoretical Investigations of Nanostructured Materials and Composites		G-AFOSR-91-0421	
6. AUTHOR(S)			
E.C. Aifantis, S.A. Hackney, W.W. Milligan			
7. PERFORMING ORGANIZATION NAME(S) AND ADDRESS(ES)		8. PERFORMING ORGANIZATION REPORT NUMBER	
Michigan Technological University Houghton, MI 49931		AFOSR-TR- 96-0001	
9. SPONSORING/MONITORING AGENCY NAME(S) AND ADDRESS(ES)		10. SPONSORING/MONITORING AGENCY REPORT NUMBER	
Air Force Office of Scientific Research Directorate of Aerospace and Materials Sciences Bolling Air Force Base, DC 20332			
11. SUPPLEMENTARY NOTES			
12a. DISTRIBUTION/AVAILABILITY STATEMENT		12b. DISTRIBUTION CODE	
Approved for public release, distribution unlimited			
13. ABSTRACT (Maximum 200 words)			
<p>An interdisciplinary research program was conducted to understand the mechanisms of deformation and fracture in nanostructured materials. Experiments on thin film nanostructured metals found that deformation occurred by grain boundary sliding and grain rotation in nanostructured gold deformed at room temperature, with grain sizes less than 25 nm. Bulk iron-copper nanostructures with grain sizes in the 100 nm size range exhibited perfectly plastic behavior and intense shear banding as the primary deformation mechanism. A variety of modeling techniques were conducted to determine the effects of grain size on strength, and to determine the constitutive behavior of nanostructured metals. Models of gradient plasticity and elasticity were also developed for traditional materials and thin films.</p>			
14. SUBJECT TERMS		15. NUMBER OF PAGES	
Nanostructured materials, constitutive equations		54	
		16. PRICE CODE	
17. SECURITY CLASSIFICATION OF REPORT	18. SECURITY CLASSIFICATION OF THIS PAGE	19. SECURITY CLASSIFICATION OF ABSTRACT	20. LIMITATION OF ABSTRACT
Unclassified	Unclassified	Unclassified	

NSN 7540-01-280-5500

Standard Form 298 (Rev. 2-89)
Prescribed by ANSI Std Z39-18
298-102

33162100661

Experimental and Theoretical Investigations of Nanostructured Materials and Composites

AFOSR 91-0421 - Final Contract Report



Elias C. Aifantis, Stephen A. Hackney and Walter W. Milligan
Center for Mechanics, Materials and Instabilities
Michigan Technological University, Houghton MI 49931

NOTICE OF PUBLIC HEARING ON THE PROPOSED
THIS IS TO ANNOUNCE THAT A PUBLIC HEARING WILL BE HELD ON THE PROPOSED
PROJECT, WHICH IS LOCATED IN THE TOWN OF STURGEON BAY, WISCONSIN, ON THE
ISSUE
DOING
STURGEON BAY, WISCONSIN, ON THE
10-12

Table of Contents

<u>Item</u>	<u>Page</u>
Executive summary	4
Personnel supported and list of publications resulting from research	5
1. Introduction	8
1.1 Background - Nanostructured materials	8
1.1.1 Structure and deformation of nanostructured materials.....	8
2. Experimental studies of deformation in nanostructured metal thin films	10
2.1 General features of deformation and fracture - nanostructured gold	11
2.2 The mechanisms of plasticity in 10 nm grain size gold	14
2.3 The mechanisms of plasticity in larger grain size (100 nm+) nanostructures	19
2.4 Discussion - Deformation of nanostructured metal thin films	20
2.4.1 10 nm grain size	20
2.4.2 Effects of grain size	21
3. Experimental studies of bulk nanostructures	22
3.1 Structure and mechanical behavior of bulk Fe-10%Cu nanostructures	22
3.2 Rapid powder forging of bulk nanostructures	25

(Continued on next page)

4. Modeling the mechanical properties of nanostructures	27
4.1 A model for the grain size dependence of the strength in nanostructured metals	27
4.1.1 Introduction	27
4.1.2 Model development	28
4.1.3 Application	29
4.2 A model for the critical grain size and strain rate necessary to obtain dislocation-based plasticity in nanostructured materials	31
4.3 A gradient elasticity model for nanostructured materials	34
4.4 A simple 1-D plasticity model for nanostructured materials	35
4.5 A 3-D phenomenological plasticity model for nanostructured materials	36
5. Modeling of material instabilities and gradient effects	38
5.1 Dislocation patterning	38
5.1.1 Dislocation patterning in crack tips	39
5.1.2 Dislocation patterning in thin films	42
5.2 Gradient plasticity	45
5.2.1 Estimates for the gradient coefficients	45
5.2.2 Size effects	46
5.2.3 Adiabatic shear banding	47
5.3 Gradient elastic fracture mechanics	49
5.4 Oscillatory fracture	50
6. References	53

Executive Summary

An interdisciplinary research effort was undertaken to understand the deformation mechanisms and constitutive behavior of nanostructured materials, as well as material instabilities in thin film and conventional materials.

Nanostructured materials are a new, exciting class of materials which have only recently been studied. They have characteristic grain sizes approximately three orders of magnitude smaller than traditional structural materials. *In situ* transmission electron microscopy was used to study deformation mechanisms of thin film nanostructured metals, in order to ascertain deformation mechanisms directly. It was found that deformation occurred by grain boundary sliding and grain rotation when thin films with grain sizes of 10 nm were deformed at low rates. Direct evidence of grain rotation was obtained by tracking angles between crystallographic planes in adjacent grains during straining. These experiments were conducted on gold at room temperature, and these types of deformation mechanisms would not be expected in coarser grain sized materials at such a low temperature. At higher loading rates, intergranular fracture occurred with little plasticity. Materials with grain sizes around 100 nm deformed by traditional dislocation-based plasticity. Bulk nanostructured metals were prepared by ball milling and HIP or forging techniques; these materials deformed by intense shear banding, and behaved in a nearly perfectly-plastic manner.

Several different types of modeling were accomplished for nanostructured materials. By considering that all metals consist of two “phases,” a boundary “phase” and a bulk “phase,” it was possible to predict the effects of grain size on strength into the nanostructured regime with a rule of mixtures approach. Such a model predicted that the strength of nanophase metals should deviate from Hall-Petch behavior at approximately 20 nm, and the strength may decrease with decreasing grain size, but only at grain sizes less than 5 nm. The model is in reasonable agreement with the available data, most of which is for grain sizes above 10 nm. A model for the grain size dependence and strain rate dependence of dislocation generation was formulated. The model considers image forces on dislocations which may be grown into a polycrystalline aggregate, or pulled from a grain boundary source. This simple model predicted that no dislocations should be present in the 10 nm grain size material, as was experimentally observed. However, at 100 nm grain size the image forces were not sufficient to remove all dislocations, and therefore the observed dislocation-based plasticity was predicted. A gradient elasticity model was derived for nanostructured materials, using the same “two-phase” material assumptions as in the earlier strength model. The model shows promise for understanding “wavy” crack paths and crack bifurcation behavior that was observed in nanostructured metal thin film experiments. Finally, two viscoplastic constitutive models were derived for nanostructured materials, based closely on the observations of grain boundary sliding and pore evolution in the thin film experiments.

Continuing research on deformation patterning and material instabilities was supported by the contract. A three-element plasticity model was derived, in which mobile (gliding) dislocations, slow moving dislocations (e.g. climbing dislocations or dipoles), and immobile dislocations interact within a reaction-diffusion kinetics framework. An important result of the model is the existence of multiple steady-state solutions of the governing differential equations. Transitions from one state to another are associated with instabilities occurring during the process of plastic deformation. The model was applied to crack tip plastic zones and thin films. The crack-tip model predicted periodic oscillations in crack tip opening displacement under certain conditions, and is applicable to situations where non-steady state crack propagation occurs. The thin film model was applied to the generation of misfit dislocations in epitaxial thin films, and predicted instabilities in the misfit dislocation structures as a function of film thicknesses and other parameters. Finally, gradient plasticity and elasticity models were refined and applied to problems related to dislocation patterning, size effects, adiabatic shear banding, fracture mechanics, and oscillatory fracture behavior in polymeric materials.

Personnel Supported

The contract supported three senior researchers at Michigan Technological University, as well as 6 graduate students and 4 visiting scientists. The senior personnel were:

Elias C. Aifantis, Professor of Mechanical Engineering and Engineering Mechanics (PI)

Stephen A. Hackney, Professor of Metallurgical and Materials Engineering

Walter W. Milligan, Associate Professor of Metallurgical and Materials Engineering

Publications

Below is a list of 30 refereed publications that were supported directly by AFOSR funding from this program. Many of the important results from these papers are summarized in this report.

Refereed Journals

1. E.C. Aifantis (1992) On the role of gradients in the localization of deformation and fracture, International Journal of Engineering Science, 30, 1279-1292.
2. S.B. Altan and E.C. Aifantis (1992) On the Structure of the Mode III Crack-Tip in Gradient Elasticity, Scripta Metallurgica et Materialia, 26, 319-324.
3. W.W. Milligan, S.A. Hackney, M. Ke, and E.C. Aifantis (1993) In Situ Studies of Deformation and Fracture in Nanophase Materials, Nanostructured Materials, 2, 267-276.
4. A.E. Romanov and E.C. Aifantis (1993) On the kinetic and diffusional nature of linear defects, Scripta Metallurgica et Materialia, 29, 707-712.
5. C.Q. Ru and E.C. Aifantis, A simple approach to solve boundary value problems in gradient elasticity, Acta Mechanica, 101, 59-68, 1993.
6. Y. Estrin, L.P. Kubin and E.C. Aifantis (1993) Introductory remarks to the viewpoint set on propagative plastic instabilities, Scripta Metallurgica et Materialia, 29, 1147-1150.

7. A.E. Romanov and E.C. Aifantis (1994) Nonuniform misfit dislocation distribution in films, *Scripta Metallurgica et Materialia*, 30, 1581-1586.
6. A.E. Romanov and E.C. Aifantis (1994) Defect kinetics in crack instabilities, *Scripta Metallurgica et Materialia*, 30, 1293-1298.
7. E.C. Aifantis (1994) Gradient effects at the micro, macro and nano scales, *Journal of Mechanical Behavior of Materials*, 5, 355-375.
8. J.E. Carsley, W.W. Milligan, S.A. Hackney, and E.C. Aifantis, (1995) Communication: Glass-like behavior in a nanostructured Fe/Cu alloy, *Metallurgical Transactions A* 26A, 2479-2481.
9. M. Ke, S.A. Hackney, W.W. Milligan and E.C. Aifantis, (1995) Observation and measurement of grain rotation and plastic strain in nanostructured metal thin films, *Nanostructured Materials* 5, 689-698.
10. J.E. Carsley, J. Ning, W.W. Milligan, S.A. Hackney, and E.C. Aifantis, (1995) A simple, mixtures-based model for the grain size dependence of strength in nanophase metals, *Nanostructured Materials* 5, 441-448.
11. M. Yu Gutkin, A.E. Romanov, and E.C. Aifantis, (1995) Nonuniform misfit dislocation distributions in nanoscale thin layers, *Nanostructured Materials* 6, 771-774.
12. J. Ning and E.C. Aifantis, (1994) On anisotropic finite deformation plasticity - Part I: A two-back stress model, *Acta Mechanica*, 106, 55-72.
13. J. Ning and E.C. Aifantis, (1994) On anisotropic finite deformation plasticity - Part II: A two-component model, *Acta Mechanica*, 106, 73-85.
14. J.M. Salazar, R. Fournet and E.C. Aifantis, (1994) Dislocation patterns induced by non-linear dislocations interactions: Spatial and temporal behavior, *Journal of Mechanical Behavior of Materials*, 5, 335-353.
15. A.E. Romanov and E.C. Aifantis, (1994) Defect kinetics in crack instabilities, *Scripta Metallurgica et Materialia*, 30, 1293-1398.
16. A.E. Romanov and E.C. Aifantis, (1994) Nonuniform misfit dislocation distributions in films, *Scripta Metallurgica et Materialia*, 30, 1581-1586.
17. J. Ning and E.C. Aifantis, (1995) On the description of anisotropic plastic flow by the scale invariance approach, *International Journal of Plasticity*, 11, 183-193.
18. H. Zhu, H.M. Zbib and E.C. Aifantis, (1995) On the role of strain gradients in adiabatic shear banding, *Acta Mechanica*, 111, 111-124.
19. T.W. Webb and E.C. Aifantis, (1995) Oscillatory fracture in polymeric materials, *International Journal of Solids and Structures*, 32, 2725-2743.
20. D.J. Unger and E.C. Aifantis, (1995) The asymptotic solution of gradient elasticity for Mode III, *International Journal of Fracture*, 71, R27-R32.

Book Chapter

21. W.W. Milligan, S.A. Hackney and E.C. Aifantis (1995) Constitutive modeling for nanostructured materials, Chapter 11 in Continuum Models for Materials with Microstructure, H. Muhlhaus, Ed., Wiley.

Conference Proceedings

22. W.W. Milligan, S.A. Hackney and E.C. Aifantis (1992) Deformation and Damage at the Nanoscale: Preliminary Observations and Modelling, in Proceedings of the ASME Symposium on Damage Mechanics and Localization, J.W. Ju and K.C. Valanis, eds, ASME, New York, MD vol. 34, 153-165.
23. M. Ke, W.W. Milligan, S.A. Hackney, J.E. Carsley and E.C. Aifantis (1993) HREM Study of fracture and deformation behavior of nanostructured thin films, MRS Proceedings, 308, 565-569.
24. E.C. Aifantis (1993) Higher Order Gradients and Self-Organization at Nano, Micro, and Macro Scales, in Continuum Models for Discrete Systems, CMDS-7, (Mat. Sci. Forum, Vols. 123-125, K.H. Anthony and H.J. Wagner, eds., Trans. Tech. Publ.
25. A.E. Romanov and E.C. Aifantis, (1994) Diffusion-like defect kinetics: Application to different plastic instabilities, in Strength of Materials (JIMIC-2, ISCMA 10), Eds. H. Oikawa et al, Japan Institute of Metals, 307-310.
26. E.C. Aifantis, (1994) Spatio-temporal instabilities in deformation and fracture, in Computational Material Modeling, AD-Vol. 42/PVP-Vol. 294, Eds. A.K. Noor and A. Needleman, ASME, New York, 199-222.
27. F. Oka, A. Yashima, T. Adachi and E.C. Aifantis, (1994) Strain and pore water pressure localization in soft clay, in Materials Instabilities - Theory and Application, AMD-Vol. 183/MD-Vol. 50, Eds. R.C. Batra and H.M. Zbib, ASME, New York, 11-18.
28. J. Ning and E.C. Aifantis, (1995) Strain gradients and size effects in composites, in IUTAM Proc. Microstructure-Property Iteractions in Composite Materials, P. Pyrz, ed., Kluwer, 223-234.
29. J. Ning and E.C. Aifantis, (1995) Anisotropic and inhomogeneous plastic flow of fibrous composites, in Micromechanics and Constitutive Modeling of Composite Materials, AMD-Vol. 202, Ed. H. Zbib, ASME, New York, 31-37.
30. E.C. Aifantis, (1995) An account of spatio-temporal instabilities in Deformation and Fracture, AMD-vol. 200, Ed. N. Ghoniem, ASME, New York, 1-7.

1. INTRODUCTION

This report summarizes the activities of an interdisciplinary group studying the mechanical behavior advanced materials, especially as related to material instabilities. The focus of the experimental studies and much of the modeling was nanostructured materials, which is an emerging class of materials exhibiting very fine structural scales and a great deal of promise. Experiments were conducted on thin film and bulk nanostructures, and Sections 2 and 3 in this report deal with these subjects. Modeling of the mechanical and constitutive behavior of nanostructures was accomplished, and is reported in Section 4. Finally, modeling studies of material instabilities in traditional materials and thin films were performed, and they are reported in Section 5.

1.1 Background - Nanostructured Materials

Nanostructured materials are a unique class of materials having characteristic grain sizes that are two or three orders of magnitude smaller than those of traditional metals or ceramics. These materials have been studied in detail only recently, since about the mid-1980's, when techniques were developed to synthesize ultra-fine, single crystalline powders. Nanostructured materials have created a great deal of interest, due to the potential of improved properties in comparison to conventional structural materials. High-toughness ceramic and intermetallic materials have been developed, along with very high strength metal alloys. Processing is improved due to improved diffusion in the nanostructured material. Increased fracture strength has been obtained in brittle materials. Physical properties, such as density and thermal conductivity, are vastly different in nanostructured materials, and both metastable phases and increased solid solubility have been reported. Several reviews of processing and properties of nanostructured materials are available [1,2]. These reviews and the references quoted therein should be consulted for further information about basic materials issues.

Since the science of nanostructured materials is in its infancy, many aspects of material structure and structure/property relations are not known. Of particular interest here are the deformation behavior of nanostructured materials, and the associated constitutive behavior. Experimental observations and constitutive models related to these issues are discussed in this report.

1.1.1 Structure and Deformation of Nanostructured Materials

A material may be considered to be "nanostructured" if the grain size is on the order of 100 nm or less. For comparison, typical engineering metals have grain sizes between 5 and 100 μm . ($1 \text{ nm} = 10^{-9} \text{ m}$, while $1 \mu\text{m} = 10^{-6} \text{ m}$.) Figure 1 shows a physical model of a nanostructured

material. Two types of atoms are present, one representing “boundary” atoms and one representing “bulk” atoms. The same two species are present in conventional materials, but only as the grain size approaches 10 nm does the fraction of “boundary” atoms become appreciable. In this range, depending on the assumed thickness of the “boundary” region, simple geometrical calculations show that the fraction of “boundary” atoms will approach that of the “bulk” atoms. Since the boundaries are more open and disordered, the material may be viewed as consisting of two “phases.”

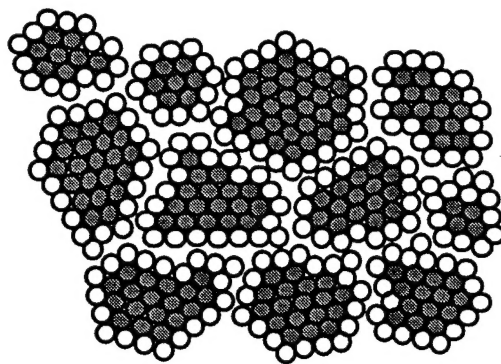


Figure 1 Schematic depiction of a nanostructured material, showing atoms which may be considered to be in grain interiors (grey) and atoms which may be considered to be in grain boundaries (white).

The relevant deformation and fracture mechanisms at the nanoscale have not been sufficiently studied, and they are not well understood. For example, while in traditional metals and alloys the strength increases and the ductility decreases as the grain size gets smaller, at grain sizes of 10 - 20 nm some studies have proposed that a “reverse phenomenon” of decrease in strength with decreasing grain size occurs [3]. More recent studies have cast doubt on this early result [4], but the difficulties associated with producing clean, reproducible nanostructured materials in bulk have made experimental studies very difficult and mechanical property measurements suspect. Moreover, as the grain size approaches 10 nm, the classical deformation mechanisms such as the operation of Frank-Read dislocation sources and the formation of dislocation pileups and cell walls become increasingly difficult and irrelevant (dislocation core size is comparable to the grain size). Most of the speculation for the pertinent deformation mechanisms has centered around the increase in interfacial area and grain boundary triple junction density leading to enhanced room temperature boundary sliding or creep, and triple junction and nanopore migration leading to irreversible plastic deformation. However, the effects of nanopore density and morphology are not known and a relevant issue is whether current theories of monolithic or composite material behavior may be extrapolated to systems where grain or reinforcement size and spacing approach the range of 10 nm or less.

2. EXPERIMENTAL STUDIES OF DEFORMATION IN NANOSTRUCTURED METAL THIN FILMS [5-7]

Since the deformation behavior of nanostructured materials is not known, experiments were conducted to determine these mechanisms and aid in constitutive modeling. A convenient means of studying deformation in nanostructures is to deform thin films *in situ*, inside a transmission electron microscope. In traditional grain size metals, care must be exercised when applying the results of such studies to bulk materials, because the film thickness is significantly smaller than the grain size. In nanostructured metal films, this is less of a concern, because the film thickness is the same magnitude or greater than the grain size. Deformation mechanisms may be observed directly, at high resolution, in an atomic resolution microscope fitted with a straining stage. The experimental studies accomplished direct observation of deformation in nanocrystalline metals and composites, with grain sizes down to 8 nm.

The geometry of the thin film experiments is shown in Figure 2. A substrate, which is aluminum, a polymer, or carbon, is coated with a nanocrystalline gold layer [5-7]. If the substrate is the polymer or aluminum, it deforms in a controlled, ductile fashion, as shown in the figure. If the substrate is carbon, the substrate is brittle and much thinner, and it tends to crack and fail at a high rate. In either case, the deformation in the coating can be viewed directly after the loading has been interrupted. By loading in steps, the sequence of deformation can be ascertained with very high resolution. The observer is looking down from the top of the film.

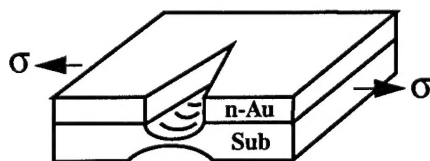


Figure 2 Schematic diagram illustrating the geometry of the *in situ* deformation and fracture experiment. A nanostructured gold coating (n-Au) on an aluminum, polymer, or graphite substrate is deformed and observed in the transmission electron microscope.

Such studies have been conducted with nanostructural gold coatings (to observe the deformation characteristics of the nanophase material), and also with brittle silica coatings (to observe the deformation and fracture of the aluminum substrate at high strains.) The major new findings of these studies, related to deformation of nanostructured gold films, may be summarized as follows: *i*) Nanostructured films deform in a ductile manner, at grain sizes down to at least 8

nm; *ii*) Plastic deformation occurs in the finest grained samples (8-25 nm) without dislocation activity; *iii*) Nanopores which are present in grain boundary triple junctions grow during deformation, by an apparently diffusive nature, even at room temperature. This is a very low temperature for gold, and large scale diffusion would not be expected in traditional grain size regimes; *iv*) Direct evidence of grain rotation and presumably grain boundary sliding during deformation of these films has been observed. Again, grain boundary sliding would not be expected in traditional gold until a much higher temperature; *v*) Nanostructured gold coatings strained at high rates (on a carbon substrate) exhibit undulated fracture surfaces with a wavelength much larger than the grain size. Details of these experimental results are presented in References [5-7]. Key results are presented below.

2.1 General Features of Deformation and Fracture - Nanostructured Gold [5]

Figure 3 shows a typical microstructure during deformation of a gold film with an average grain size of 8 nm. In this case the gold film was deposited on top of aluminum, and similar results were obtained when the gold was deposited on a thin polymer substrate (which would have little effect on the deformation characteristics of the gold coating.) In the micrograph, the observer is looking down, perpendicular to the film which is being strained in the plane of the paper.

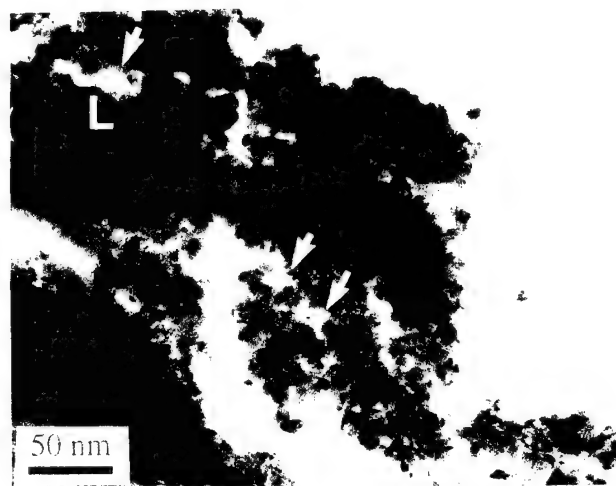


Figure 3 TEM micrograph showing extensive plasticity, ligament formation, and crack growth by void coalescence and link-up in nanocrystalline gold (8 nm grain diameter) on Al substrate.

Several important observations may be elucidated. First, *the nanocrystalline gold deformed in a very ductile manner*. This is clearly observable by examining the mating gold crack faces in the secondary cracking region; the material adjacent to the crack faces has deformed extensively, and the crack faces do not "mesh" as they would in the case of brittle fracture.

Additionally, one may observe ductile ligaments which are bridging the secondary cracks (indicated by "L's" in the figure). These ligaments are necking and deforming permanently as the crack tip opening displacement increases. Figure 3 also shows evidence of crack growth by microvoid coalescence and link-up. These "nanopores" are indicated by arrows, and appear to be growing along the grain boundaries. This leads to a grain boundary "grooving" effect which can be clearly observed in the nanopores in the figure. [For example, the pore above the uppermost "L" is not symmetric; it is semicircular on top, but a grain boundary groove has formed on the bottom.] It is difficult to imagine this type of void growth and grain boundary grooving occurring without the aid of extensive diffusion, even though the homologous temperature is very low. The cracks observed in Figure 3 grew along the grain boundaries, apparently due to the growth and link-up of grain boundary voids.

This growth of grain boundary nanopores has been directly observed in atomic resolution microscopy. Figure 4 shows a sequence of micrographs taken during crack growth in a nanostructural gold film. Ahead of the crack tip, a nanopore nucleated, Figure 4(a). Under further loading, the pore grew until only a ligament separated the pore from the crack, Figure 4(b). The ligament connected two different grains and narrowed until it pinched off at the grain boundary. After pinching off, the ligament rapidly disappeared to produce a grain surface of uniform curvature, Figure 4(c).

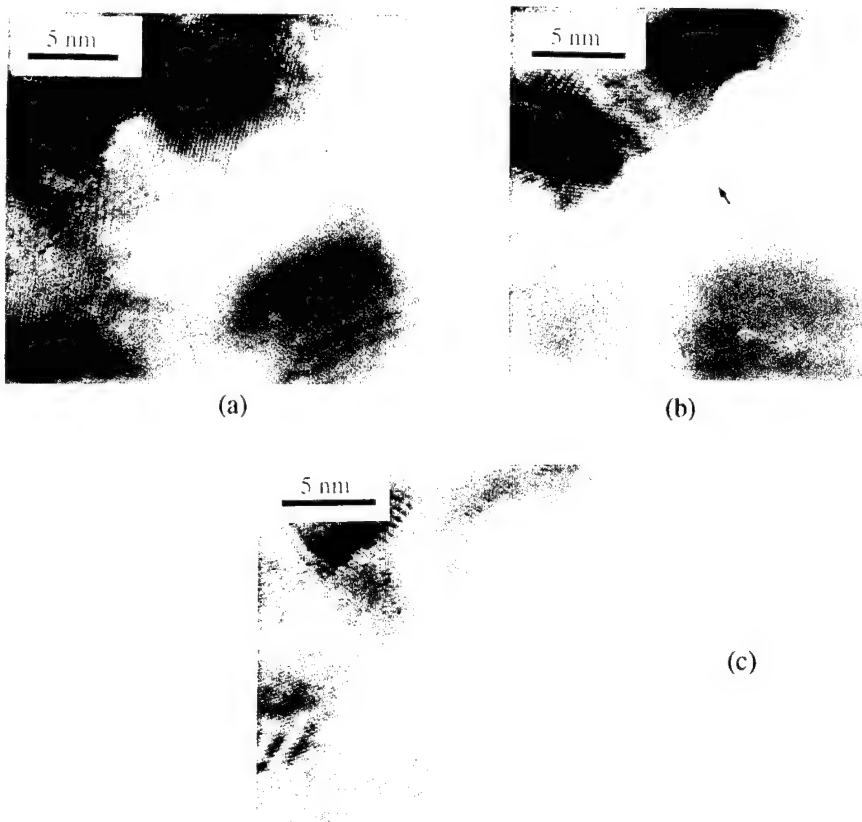


Figure 4 Lattice-image micrographs of *in situ* crack propagation in 8 nm grain diameter gold on a thin carbon substrate. (a) Intergranular crack propagation and nanopore formation in the grain boundaries ahead of the crack tip. (b) Crack growth and ligament formation. (c) Diffusion-based elimination of the ligament.

The shape changes just described occurred without any apparent dislocation activity within the ligament. The smoothing of the ligament after pinching off at the grain boundary is certainly a diffusive process, and it is proposed here that the thinning of the ligament itself is caused by mass diffusion. A natural question which arises is whether this ligament formation and diffusion-based deformation is a thin-film effect or an artifact of the TEM environment. Although surface diffusion may be a factor, temperature probably is not, as previous investigators have determined that beam-heating of thin foils is limited to about 100°C. Furthermore, *in situ* straining experiments on coarse-grained materials [8] have resulted in ligament formation during ductile fracture, but this ligament formation was always associated with dislocation activity. Therefore, the observations of diffusion-based deformation in these nanometer grain size thin films cannot be ascribed to thin film effects alone; the grain size and atomic structure must be significant factors.

A final observation concerning fracture regards periodic instabilities observed in 25 nm grain size gold films on carbon substrates. Figure 5 shows that the crack path became undulated, in an almost sinusoidal shape, after which crack bifurcation occurred. The wavelength of the crack undulation is significantly larger than the grain size.

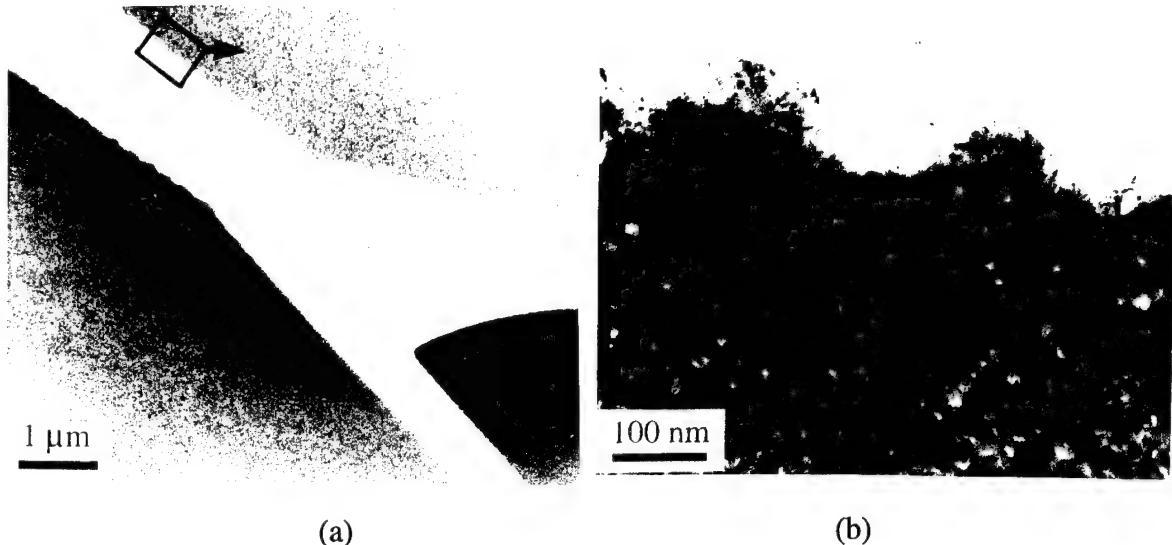


Figure 5 Plastic deformation and fracture of 25 nm grain diameter gold film on carbon. (a) TEM micrograph showing periodicity before crack bifurcation. (b) Higher magnification TEM micrograph showing periodicity of crack path and plastic thinning along crack face.

2.2 The Mechanisms of Plasticity in 10 nm Grain Size Gold [6]

As noted above, there was no experimental indication of dislocation activity within individual grains. That is, no dislocation images were observed within the grains after straining, and no contrast changes associated with moving dislocations were observed on videotape during *in situ* straining. This suggests that the ductile behavior was due to grain boundary processes such as grain boundary sliding.

The deformation behavior was studied in the thin films, in the region ahead of a growing crack tip. The {111} and {200} lattice fringe images are easily observed for properly-oriented grains. These fringes lie parallel to the trace of the respective crystal planes. Because of the small scattering angle for electron diffraction, fringe images are expected to be observed only for those crystal planes with normals approximately perpendicular to the incident beam direction. Thus, a misorientation angle is specified in the image plane (corresponding closely with the film plane)

for two nanocrystals with observable lattice fringes. A change in the misorientation between two grains by rotation is then observable by a change in the angle between the lattice fringes. This technique works very well, as long as the axis of rotation is nearly parallel to the electron beam and film normal; otherwise, the lattice fringes will go out of contrast as the diffracting planes are rotated away from the beam. It has been our experience that during deformation, lattice fringe contrast may change in some grains but not others, and that the loss of lattice fringe contrast in a given grain may be transient.

An example is shown in Figure 6, in which a crack is growing from left to right in the micrograph and lattice fringes are imaged in most grains. The angles between the lattice fringes among several grains (labelled with letters in Figure 6) were measured at successive straining stage displacements. The grain misorientation angle between most of these grains was altered during deformation, indicating that the grains underwent a relative rotation with respect to each other. The relative rotation of the of the lattice fringes from two typical grains is shown in Figure 7.

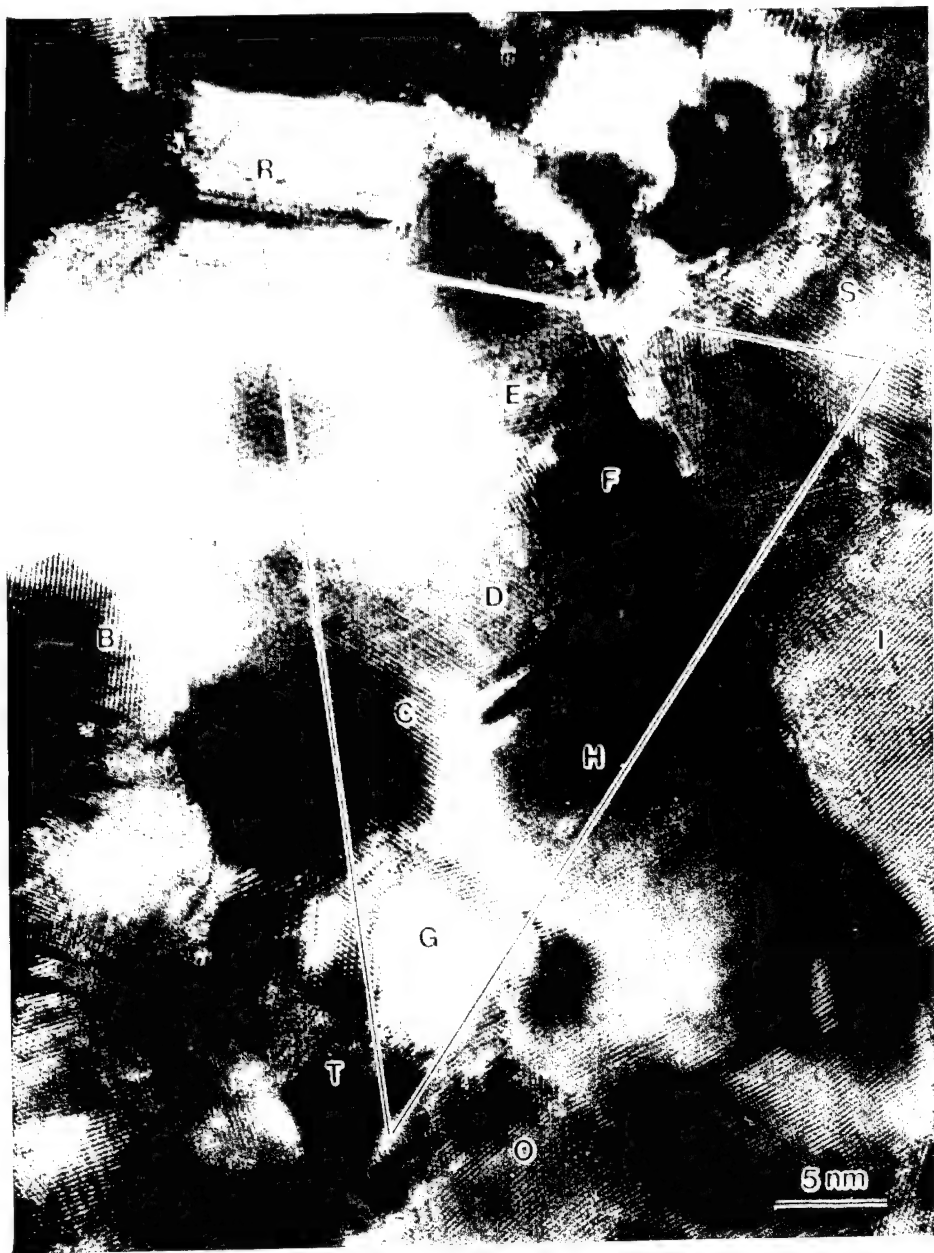


Figure 6 High resolution lattice image of grains ahead of a crack tip, growing from left to right in the top half of the photo. 8 μm macroscopic displacement.

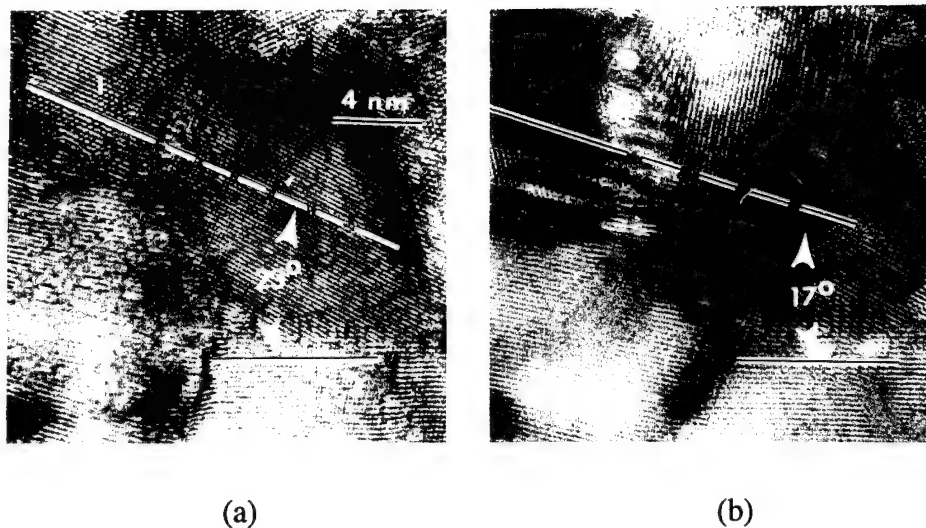


Figure 7 High resolution lattice images in the same area as Figure 6, showing a 6 degree change in the angle between lattice fringes of neighboring grains during straining. The grains being measured are labelled 1 and 2. (a) Before straining. (b) After 25 μm macroscopic displacement.

The rotations observed for representative grains are given in Table I and plotted in Figure 8(a). The sign convention is as follows: the lattice fringes in Grain I define a material reference axis, and a counter-clockwise rotation of any grain with respect to the fringes in Grain I is arbitrarily defined as a positive rotation. Several interesting conclusions may be drawn from this data. First, significant relative rotations occurred; Grains F and I, which are separated by only one grain, rotated 15 degrees with respect to each other. Second, the rotation was inhomogeneous; for example, adjacent Grains C and D did not rotate at all, while adjacent Grains D and F rotated by 7 degrees. Finally, the measurements are self-consistent within approximately 2 degrees; that is, the rotations of pairs CI and DI are equal, and the sum of the rotations of pairs DF + DI are within 2 degrees of the rotation of pair FI, as is required by geometry.

Table 1: Relative rotations of representative grains during straining

Displacement, μm	Relative rotation between grain pairs, degrees				
	CD	DF	DI	CI	FI
1	*	1	-1	-1	0
2	0	*	*	*	-1
6	*	*	*	5	4
8	-1	4	4	5	10
25	0	7	6	6	15

* = insufficient lattice image contrast for accurate measurement

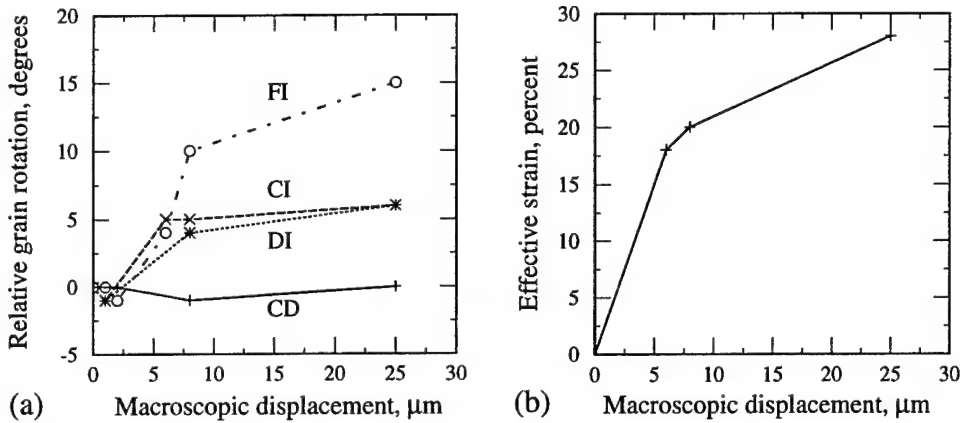


Figure 8 Grain rotation and plastic strain during in situ loading. (a) Relative changes in angle during deformation between representative pairs of grains shown in Figure 6, as a function of displacement of the straining stage. Accuracy of measurement is ± 2 degrees. (b) Effective plastic strain measured in the same area.

The observation of grain rotation may imply the occurrence of strain via grain boundary sliding. Thus, it is of interest to determine the local strain tensor and the level of plastic strain associated with the deformation. Tensile loading of a cracked thin film is a plane stress situation, which simplifies the analysis. Therefore, the 2-D strain tensor may be determined by measuring the change in shape of a triangle in the deforming zone. By measuring the change in length of the sides of the triangle, an indication of normal strain in three different directions is obtained. This is analogous to a standard mechanical engineering "strain gage rosette" technique for measuring strains in a plane, and elementary relations are available for determining the strain tensor in two dimensions from the three independent normal strain measurements [9]. This technique should give a good approximation of the 2-D strain tensor when the changes in angle between the sides of the triangle are small. If elastic strains are much smaller than plastic strains, constancy of volume can be assumed, requiring that the sum of the normal strains must be zero. This allows the calculation of the normal (Poisson) strain in the direction of the film normal. A simple, scalar indication of the extent of plastic deformation is the "effective strain", which can be easily calculated from the plastic strain tensor [10]. In uniaxial tension, the effective strain is equal to the plastic strain.

The difficulty in applying the technique described above lies in identifying three material points which can be unambiguously tracked during displacement of the straining stage. In the first analysis, the triangle shown in Figure 6 was used to determine the strain tensor. The corners of the triangle were the areal center of Grain S, and the centers of identifiable twins in Grains T and R. A second triangle, using grain boundary triple junctions in the same general area, yielded essentially the same results. With respect to a Cartesian coordinate system in which the foil normal is parallel to z , the crack is propagating along x , and the stress is being applied along y , the

following strain tensor was calculated (using the triple junction triangle) for the complete deformation sequence (25 μm macroscopic displacement):

$$\tilde{\boldsymbol{\epsilon}} = \begin{bmatrix} 0.05 & -0.11 & 0 \\ -0.11 & 0.19 & 0 \\ 0 & 0 & -0.24 \end{bmatrix}$$

It is difficult to assess the accuracy of this strain tensor. There are inevitable errors in identifying the same material point from step to step, which is necessary for placing the triangle. This is the major source of error. The measurement of the lengths of the triangle sides and angles will introduce further error. Finally, there is likely a stress gradient in the zone of interest ahead of the crack tip, and the analysis assumes uniform strain. Due to all of these uncertainties, the above-determined strain tensor must be viewed as a first approximation only. At this level of accuracy, the rosette-like analysis is a reasonable means for measuring the strain tensor. Confidence in this approach was developed further by comparison with a rigorous analysis, including finite plasticity and determination of the rotation tensor, which gave essentially similar results.

The effective strain associated with the above plastic strain tensor is 28%. Even with the uncertainties in strain determination, it is clear that large plastic strains occurred, and that the plastic strain was much larger than the elastic strain. The effective strain is plotted against macroscopic displacement in Figure 8(b). The trends are consistent with the observed grain rotations (Figure 8(a)), in that the relative grain rotations and the effective plastic strains both changed much more rapidly in the first 8 μm of macroscopic displacement than in the final 17 μm .

2.3 The Mechanisms of Plasticity in Larger Grain Size (100 nm+) Nanostructures [6]

Thin films with larger grain sizes were prepared by evaporation. Due to significant advantages in ease of film preparation and in the quality of the films, silver was used for this portion of the research instead of gold. In thin films with grain sizes around 110 nm, dislocations were observed both during and after *in situ* straining. An example is shown in Figure 9, in which a silver film with a grain diameter around 110 nm was strained until the film necked and fractured. Figure 9(a) shows a number of dislocations present in the vicinity of the neck, as observed by strain contrast, while Figure 9(b) shows a single dislocation present in the neck, as observed by lattice fringe contrast. Dislocation motion was also evident on video images obtained during the straining process. These experiments confirm that dislocations will be found in the *in situ* straining experiments if they are present, and therefore verify that there was no dislocation activity in the 10 nm grain size films.

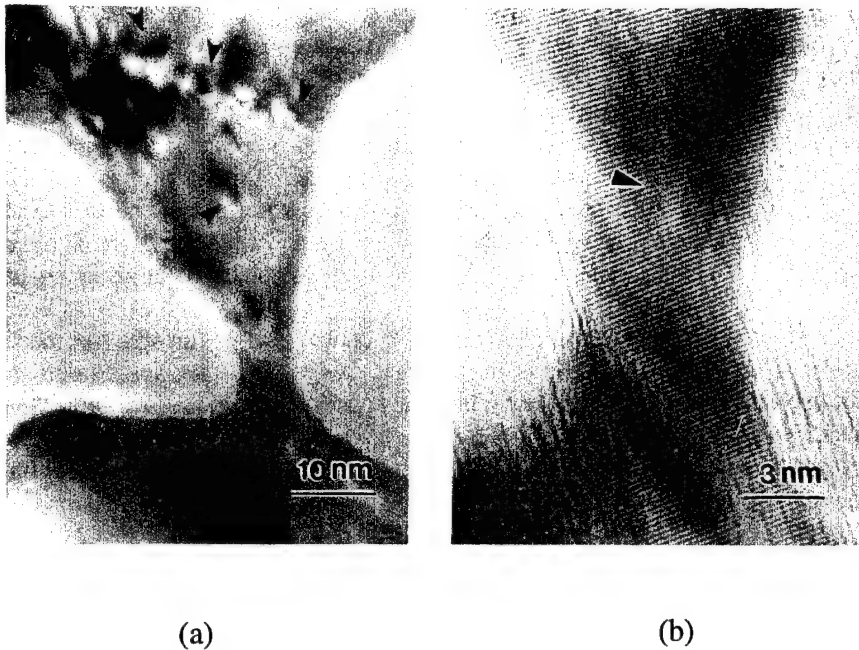


Figure 9 Dislocations present after straining a silver film with 110 nm grain size. (a) Multiple dislocations, observable by strain contrast. (b) A single dislocation, observable by lattice fringe contrast.

2.4 Discussion - Deformation of Nanostructured Metal Thin Films [6]

2.4.1 10 nm grain size

It is apparent that significant plastic strain occurred simultaneously with the observed grain rotations. These observations are similar to the behavior observed in larger-grain superplastic alloys deformed at elevated temperature. Investigators who study superplasticity generally believe grain rotation is a result of unbalanced shear stresses associated with inhomogeneous grain boundary sliding.

The rotation axis of most of the grains was essentially parallel to the film normal. This is clear because the lattice fringes remained visible after large relative rotations in the film plane, implying that there were no significant rotations which would cause a large change in the Bragg deviation parameter for the lattice planes being imaged. The observation that the grain rotation axis was perpendicular to the film implies that these rotations occurred in response to the applied stress, not to reduce surface energy, grain boundary energy, or in response to some other unspecified driving force.

The magnitude of grain rotation was inhomogeneous, as seen in Figure 8. Two possible reasons for this behavior are that the grain boundary structure was not conducive to grain boundary sliding, or that the grain shapes inhibited the rotation process. In any case, the

experimental observation suggests that strain inhomogeneities may be present to the extent that local grain boundary fracture processes may be induced. This is consistent with the observation of multiple crack formation in nanocrystalline films with 'pore' formation and growth occurring at triple junctions [5].

The extensive grain boundary sliding, leading to grain rotation, is an effective mechanism of stress relaxation. At this small rate of macroscopic displacement and small grain size, the majority of the plastic strain appears to occur by grain boundary processes. If the contribution of grain boundary sliding to the plastic strain is large, the local stress may not exceed the stress required to generate mobile dislocations inside the grains. The lack of experimentally observed dislocation activity certainly suggests that the stress never exceeded the yield point of the individual grains.

2.4.2 *Effects of grain size [6]*

At 10 nm grain size, no apparent dislocation activity was observed and fracture was intergranular, while at 110 nm grain size significant dislocation activity occurred and fracture was transgranular. Further work is in progress to identify the transition grain size. The observation of dislocation activity in the larger-grained films is important, because it verifies that there is no experimental difficulty in imaging dislocations in these nanostructured thin film straining experiments when dislocations are present.

It may be argued that nanostructured metals deform by very rapid dislocation activity, in which dislocations sweep from grain boundary to grain boundary almost instantaneously, thus precluding direct observation. While this may or may not be the case in bulk nanostructured metals, it is difficult to imagine that such a mechanism could occur in thin films like the ones studied here without significant and experimentally-measurable consequences. Plastic strains around 30%, along with relative grain rotations up to 15 degrees, were observed. The grain rotation axis was normal to the foil, and only minor changes in grain shape occurred. In the absence of grain boundary sliding, this deformation would require the motion of a large number of dislocations, with a special distribution of Burgers vectors and slip planes. Presumably, at least a small fraction of these dislocations would be trapped in the grains during deformation, due to dislocation intersection processes if nothing else. Since no evidence of dislocation activity has been found in numerous experiments, it is likely that no significant intragranular dislocation activity occurred in these 10 nm grain size, thin film specimens.

In summary, it was found that nanocrystalline gold films with grain sizes from 8-25 nm deform at room temperature in a ductile manner. However, dislocation motion is not responsible for the deformation, as it would be in traditional grain size gold. Instead, diffusion, pore growth, grain boundary sliding and grain rotation appear to be responsible for the plasticity. Some question remains as to whether this thin film behavior is representative of bulk behavior.

3. EXPERIMENTAL STUDIES OF BULK NANOSTRUCTURES

While the thin film experiments described above are of fundamental interest for determining deformation mechanisms, and are of interest in the areas of microelectronics and coatings, they are not structural materials. The production of bulk nanostructures for load-bearing components has been problematic for the entire materials community. The production of nanostructures is only possible in processes occurring far from equilibrium, by techniques such as gas condensation, ball milling, or thin film deposition. The product is a powder or thin film that must be consolidated. Consolidation of powders generally requires time at high temperatures, which coarsens the grain size catastrophically.

In this research, two techniques have been utilized to avoid catastrophic coarsening during consolidation. First, a two-phase system (Fe/Cu) which phase-separates has been chosen for initial studies; this type of system allows for pinning of grain boundaries by the minor phase, resulting in less coarsening. Second, rapid powder forging techniques have been adopted to fully consolidate nanostructured powders in a very short time at high temperature. The details are reported in References [11,12].

3.1 Structure and Mechanical Behavior of Bulk Fe-10%Cu Nanostructures [11,12]

Mechanical ball milling was used to produce nanostructured powder particles with grain sizes around 15 nm. (Smaller grain sizes, down to 4 nm, have been obtained by others with this technique.) A 90% iron - 10% copper alloy was studied, because copper is insoluble in iron. The structure which results after consolidation consists of copper precipitates on the iron grain boundaries, and these precipitates impede grain growth during processing. Consolidation of the powders into bulk materials was accomplished by hot isostatic pressing (HIP) and forging. The forging technique, which is more promising than the HIP technique because it is faster, is under development presently and is discussed in the next section.

Alloys HIP'ed at 600 and 700°C for 30 minutes at 170 MPa were fully dense. As expected, the grain size coarsened substantially from the original 18 nm size. The final average grain sizes were approximately 100 nm after a 600°C HIP and 130 nm after a 700°C HIP. While significantly coarser than the 10 nm grain-size materials discussed above, these materials are still much finer than traditional steels, and may be considered to be in the upper range of "nanostructured materials."

The mechanical and deformation behavior of these materials were quite surprising; essentially, they behaved in an elastic-perfectly plastic manner. This is demonstrated in the stress strain curves of Figure 10. In this figure, the iron material had much coarser grain size than the alloys, and it exhibited traditional strain-hardening behavior. The nanostructured alloys, however,

exhibited either no strain hardening or softening upon yield.

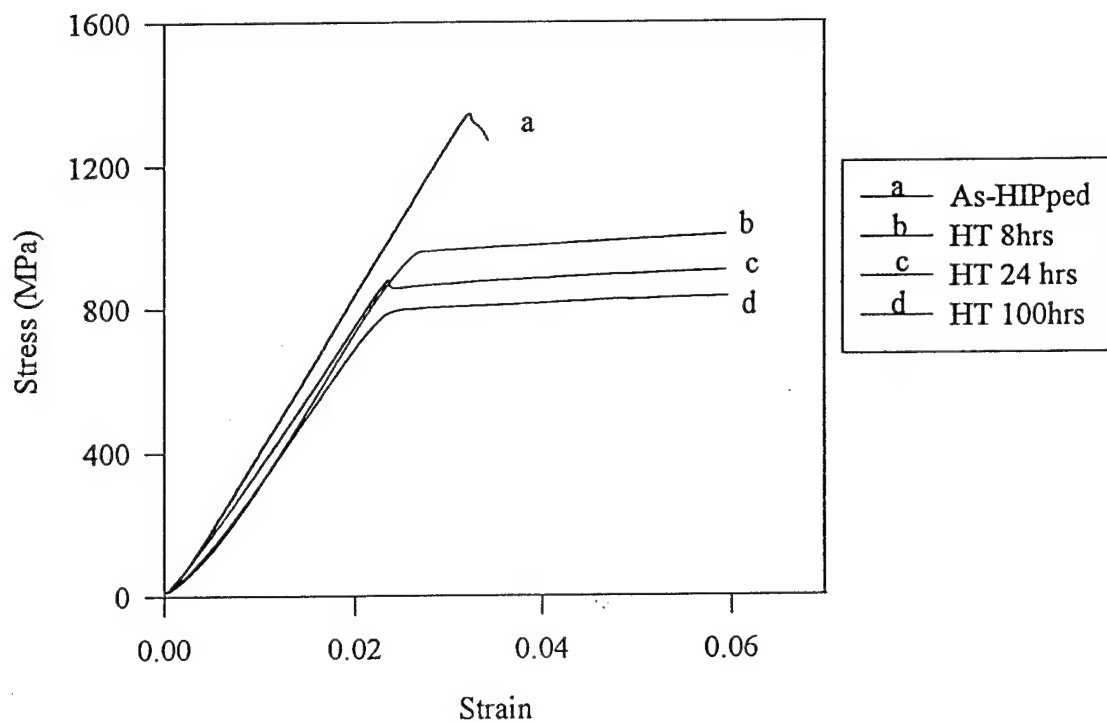


Figure 10 Stress-strain curves obtained in compression, nanostructured Fe/Cu alloys.

The deformation mechanisms observed were also quite surprising. The first mechanism of plastic deformation was intense shear banding. Shear banding at the yield point was observed at all grain sizes investigated, from 100 nm to around 650 nm. As the grain size increased, the strength decreased and the shear band width increased. Typical shear bands from representative specimens are shown in Figure 11.

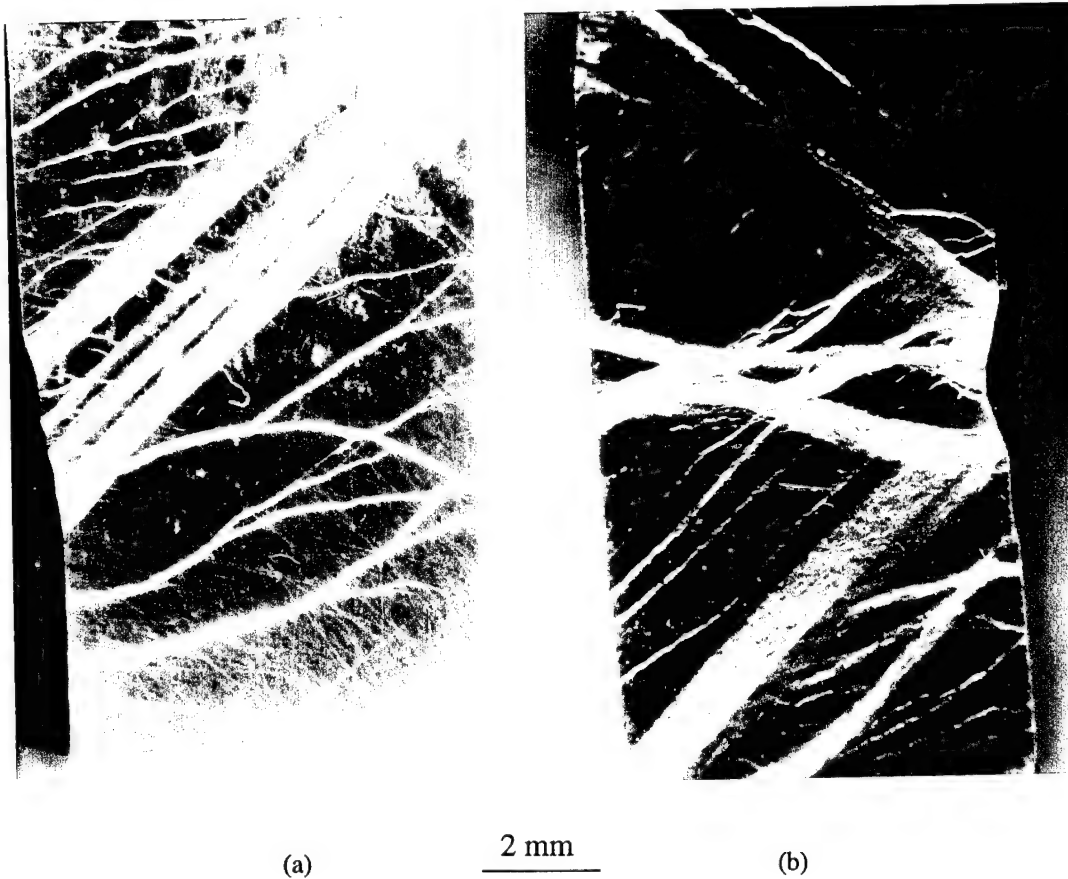


Figure 11 Massive shear bands observed on surfaces of compression specimens. (a) 100 hour heat treatment, grain size approximately 500 nm. (b) 500 hour heat treatment, grain size approximately 650 nm.

The observation of shear banding as the first mechanism of permanent deformation, at static strain rates, appears to be unique among metals. Shear banding is normally observed at very high strain rates, and/or after large amounts of cold work, but not in annealed metals at slow strain rates. This behavior is observed, however, in amorphous polymers and metallic glasses [11]. This commonality of behavior between the nanostructured metals and amorphous materials is intriguing, and is being studied currently. Another interesting point is that the grain sizes present in these nanostructured alloys are on the same order of magnitude as the *sub-grain* size which is typically obtained before cold-worked metals begin to undergo shear-banding instabilities. This similarity may be a key in understanding shear banding, both in nanostructured metals and heavily cold worked metals.

The mechanism of plastic deformation inside the shear bands is a topic of continuing study. Transmission electron microscopy of shear-banded material has revealed that the deformation within the bands is intense, while there is no deformation outside the bands. Figure 12 shows transmission electron microscope photos of a nanostructured iron alloy HIP'ed at

600°C, with an average grain size around 100 nm. In Figure 12(a), the grains maintain their original structure, while in Figure 12(b), the grains have been deformed and elongated to an aspect ratio of about 10:1. These photos were taken in adjacent regions of the same specimen, approximately 10 μm apart, giving lucid evidence of the localized deformation mechanism which is occurring.

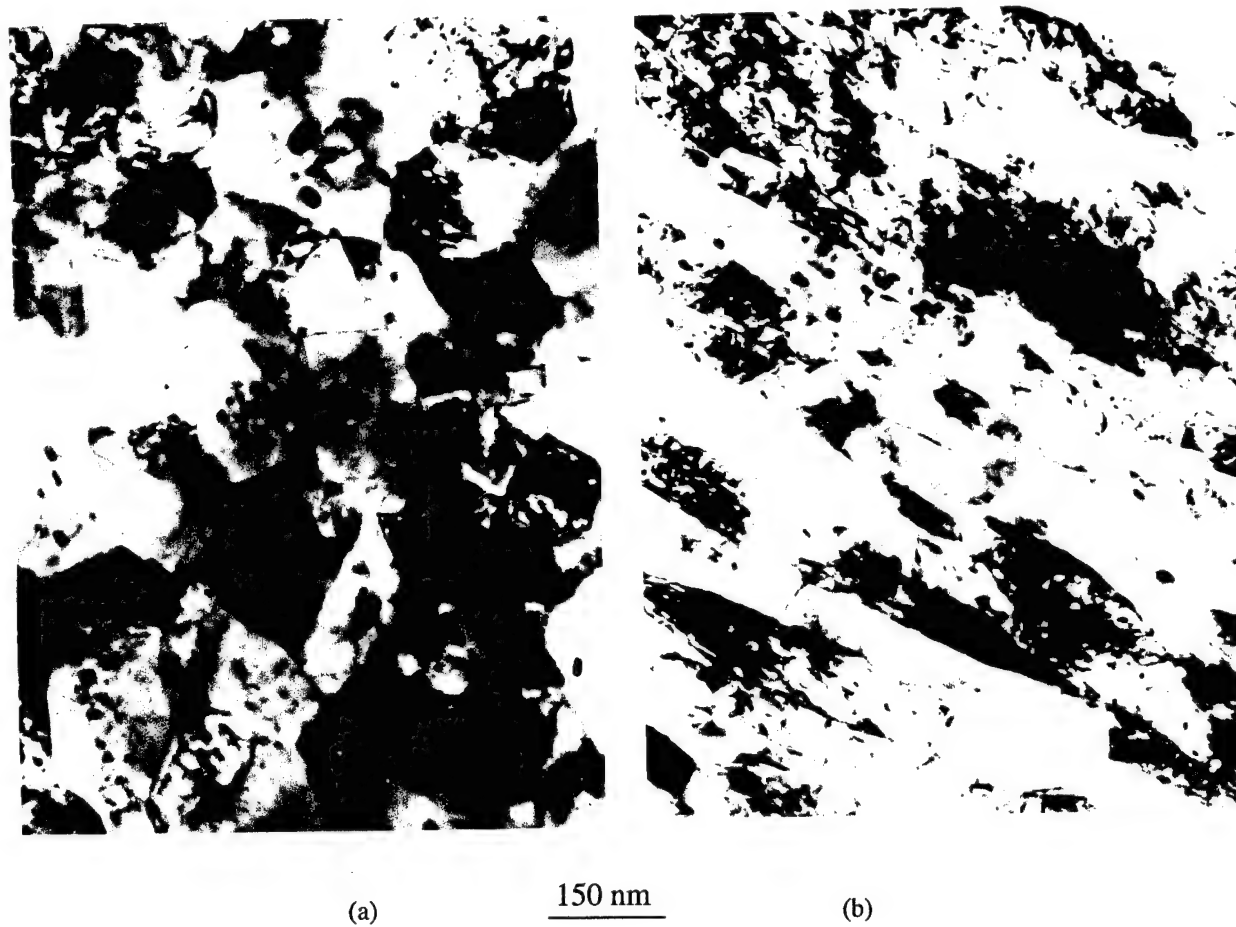


Figure 12 Transmission electron micrographs of shear banding in approximately 100 nm grain size Fe-10% Cu. (a) undeformed region. (b) highly deformed region about 10 μm away from the region shown in (a).

3.2 Rapid Powder Forging of Bulk Nanostructures

The HIP techniques were not able to consolidate Fe/Cu materials to full density without coarsening the grain size to a minimum of 100 nm. Further, the lack of shear deformation in the isostatic press precludes the shear flow necessary to heal processing defects. Therefore, rapid powder forging was evaluated as a consolidation technique at the end of this program.

Nanostructured iron/copper powders were cold pressed to approximately 90% density with a uniaxial pressure of 700 MPa at room temperature in a disposable 316 stainless steel die. The die was a cylinder, with a 25 mm outside diameter and a 12 mm inside diameter, along with a lower disk and a plunger made of a nickel-base superalloy. Cold pressing was conducted in the same argon glove box that mechanical milling and storing of the powders were done in, to avoid contamination and oxidation. The same die was transferred quickly to an argon-filled chamber in a servohydraulic loading frame. The entire die/powder assembly was rapidly heated under argon with an induction heater to temperatures between 500-700°C, and then pressed at 500 MPa and quickly cooled. The time at temperature was less than 2 minutes, as compared to approximately 40 minutes in the HIP. The specimen processed at 700°C, which is the only one which has been evaluated to date, was fully dense. The hardness of this specimen was approximately the same as the specimen which was HIP'ed at 100°C cooler, indicating that the grain size was approximately 100 nm. Current research is exploring lower temperature forging processes, in the hopes of obtaining fully-dense materials with grain sizes in the 50 nm regime.

4. MODELING THE MECHANICAL PROPERTIES OF NANOSTRUCTURES

Modeling has been approached in an interdisciplinary environment, from several different points of view. Presented below are: a model for the grain size dependence of the yield strength of nanostructures, a model for the critical grain size and strain rate necessary for dislocation-based plasticity in nanostructures, a gradient elasticity model for nanostructures, and two plasticity models for nanostructures.

4.1 A Model for the Grain Size Dependence of the Strength in Nanostructured Metals [13]

4.1.1 *Introduction*

The strength of conventional polycrystalline metals follows an empirical relationship with decreasing grain size according to the Hall-Petch equation [14-16]:

$$\sigma = \sigma_o + \beta'' d^{-1/2} \quad (1)$$

where σ is the yield stress, σ_o is the lattice friction stress, β'' is a material constant, and d is the grain size. The Hall-Petch relation (HPR) also applies to the flow stress (σ_f) and hardness (H) dependence of grain size for a given strain [16]:

$$\sigma_f(\epsilon) = \sigma_{f_o}(\epsilon) + \beta'(\epsilon) d^{-1/2} \quad (2)$$

$$H = H_o + \beta d^{-1/2} \quad (3)$$

Recent work in the area of ultra-fine grained and nanocrystalline materials [13] has demonstrated that the slope of the HPR, β , decreases significantly for grain sizes below one micrometer. Some investigations [13] have even reported a negative slope, or a decrease in flow stress with decreasing grain size; i.e. "grain size softening." Many attempts have been made to explain this anomalous behavior.

As several researchers have indicated, the effects of increased grain boundary volume fraction may cause the change in slope of the HPR, since the volume fraction of the interfaces in nanostructures becomes comparable to that of the grain interiors. This prompted Aifantis [17] to propose viewing a nanostructured material as a superposition of two continuously distributed states: the "bulk" or grain interior state and the "grain boundary" state. The two states support their own displacement and stress fields and interact via the exchange of mass and momentum, but the overall continuum is restricted to obey the standard laws of continuum mechanics. This

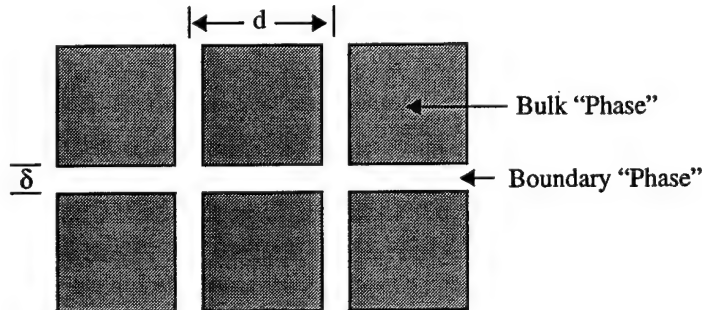
view implied that the elastic behavior at the nanoscale should be modeled by a gradient theory of elasticity, while a rule of mixtures approach could be employed to express the overall flow stress of the nanostructured material as a properly weighted average of the flow stresses of the “bulk” and “grain boundary” phases. It was further illustrated that this rule of mixtures relation for the overall flow stress can be used in principle to interpret the abnormal behavior of the flow stress on the grain size at the nanoscale. Below is a simple model based on that latter concept and provides experimental support for its validity.

4.1.2 Model Development

If a polycrystalline material is regarded as a two-phase material with a grain boundary “phase” and a bulk “phase,” as shown in Figure 1 and idealized in Figure 13, a mixture approach can be used to describe the general dependence of flow stress on grain size from the microscale down to the nanoscale regimes, regardless of the type of active deformation mechanism.

No assumption is made concerning uniqueness of the grain boundary structure or thickness in nanostructured materials; it is assumed to be a thin, relatively disordered region just as in traditional materials. The volume fraction, f , can be modeled using simple geometric shapes to describe the nanostructure.

Figure 13
Material Model.



For the two-dimensional square microstructure shown in Figure 13, the area fraction of the grain phase is:

$$f = \frac{(d - \delta)^2}{d^2} \quad (4)$$

where δ is the thickness of the grain boundary.

Regarding the polycrystalline material as a composite material consisting of a disordered grain boundary phase and a crystalline grain phase as in Figure 13, the strength can be modeled as:

$$\sigma = f\sigma_g + (1-f)\sigma_{gb} \quad (5)$$

where σ_g and σ_{gb} are the flow stresses of the bulk and grain boundary phases respectively, and f is the volume fraction of the bulk phase.

As a first approximation, the strength of the bulk phase may be described by the Hall-Petch relationship, Equation 1. This is a good approximation for a large range of grain sizes. However, as discussed above, dislocation activity is not apparent as the grain size drops below about 25 nanometers. Since the Hall-Petch relationship is based on intragranular dislocation activity, the theoretical shear strength of the material might be a better approximation of the strength of the bulk phase in this fine-grain regime. For this simple model, however, we will assume that the Hall-Petch relationship is an adequate approximation of the strength of the bulk phase over the entire range of grain sizes. Although not theoretically justified at the smallest grain sizes, this assumption keeps the model attractively simple.

The flow stress of the grain boundary phase is not known, since it is impossible to produce and mechanically test a grain boundary specimen. It is reasonable to assume that the grain boundary strength should be related to the strength of an amorphous metal, due to the relatively disordered nature of the boundary. Thus for a metallic glass-producing system, the boundary strength could be reasonably approximated as the strength of the amorphous state. It was assumed that its value, σ_{gb} , was a constant that is discussed in detail in Reference [13].

4.1.3 Application

The model was applied to three metallic systems in which data are available in the nanostructured regime and in the traditional Hall-Petch regime. The important parameters in the model are the Hall-Petch constants, the strength of the grain boundary phase, and the thickness of the grain boundary. Hardness data are available for some of the materials, and flow stress data are available for others. For consistency, and for comparison to hardness data on nanostructured materials, flow stress values were converted to hardness. After evaluating the appropriate constants [13] and combining Equations 1-5, the model is

$$H = \frac{(d-\delta)^3}{d^3} (H_o + \beta d^{-1/2}) + \frac{3d^2\delta - 3d\delta^2 + \delta^3}{d^3} \left(\frac{\mu_{cr}}{12} \right) \quad (6)$$

where δ is the boundary thickness and μ_{cr} is the isotropic shear modulus of the crystalline metal. Figure 14 shows plots of the model (Equation 6) along with data from the literature for three different metals, using 1 nm for δ .

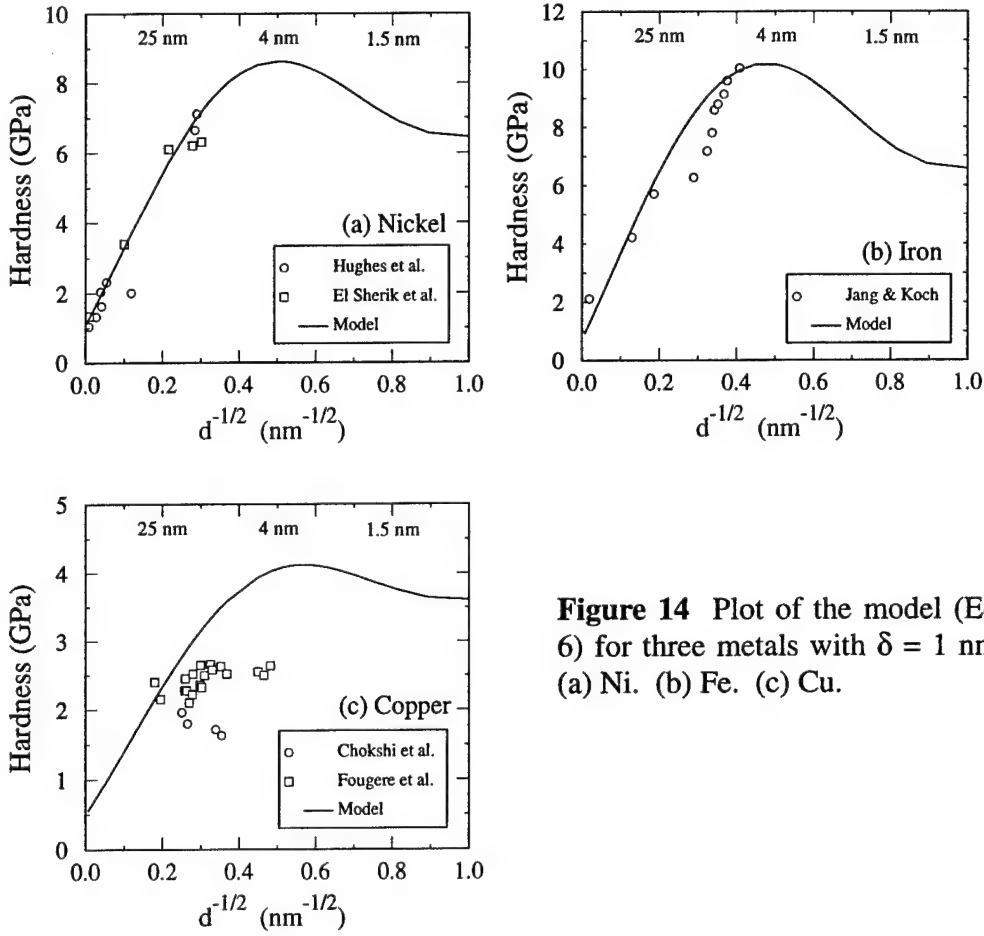


Figure 14 Plot of the model (Eq. 6) for three metals with $\delta = 1$ nm. (a) Ni. (b) Fe. (c) Cu.

The model correctly predicts the general shape of the curves for all three metals, and correlates the available data quite accurately in the cases of nickel and iron. For copper, the model correlates the shape of the curve obtained by Fougere et al. [18], and clearly predicts that the negative slope observed by Chokshi et al. [3] should not occur until much smaller grain sizes. It should be noted that the data of Chokshi et al. [3] was obtained by heat treating as-consolidated materials to coarsen the grains. This annealing resulted in simultaneous strengthening and coarsening. Most other studies, comparing either as-compacted materials to each other or heat treated materials to each other, have shown a flattening of the curve at around 10 nm, similar to the Fougere et al. data.

The model over-predicts the strength of nanostructured copper observed by Fougere et al. [18]. Although not discussed in their copper paper [18], similar nanostructured materials prepared by the same group ([19] using identical techniques resulted in porous materials with densities averaging 86%. These investigators have discussed the possibility that the porosity reduced the apparent hardness of their materials, and so it is quite possible that fully-dense nanostructured copper would exhibit hardness versus grain size behavior which is much closer to the model prediction in Figure 14(c).

In general, the model predicts that the Hall-Petch relation should be a good estimate of the strength down to about 10 nm, in agreement with the iron and nickel data. The peak strength is predicted to occur at grain sizes around 5 nm for iron, nickel and copper. Experiments in the range from 0 to 10 nm are necessary to verify the form of the model.

4.2 A Model for the Critical Grain Size and Strain Rate Necessary to Obtain Dislocation-Based Plasticity in Nanostructured Materials [20]

As discussed in Section 2, there was a transition in deformation mechanisms in the nanostructured metal thin films as a function of grain size. Below 25 nm, dislocations were not present, and fracture was observed to occur along the grain boundaries. However, above 100 nm grain size films show traditional deformation mechanisms usually observed in large grain size materials; that is, extensive dislocation activity which induces plastic thinning, ligament formation and ductile fracture within an individual grains. The strain rate in both cases was slow, $\sim 10^{-4}/\text{s}$. The purpose of this section is to examine the change in deformation mechanism which was observed between specimens with a 10 nm grain size and specimens with a 100 nm grain size. Given that the strain rates for the deformation experiments on the large and small grain materials are essentially the same, a key question is what role that grain size might play in this phenomenon.

There are indications that the local stresses are quite high during the deformation of the 10 nm materials. Small pores ($\sim 1 \text{ nm}$) are observed to open up at the grain boundary triple junctions located just ahead ($\sim 50\text{-}100 \text{ nm}$) of the crack tip [5,20]. These pores appear to be what are referred to as r-type cavities [21], known to occur as a result of grain boundary sliding. Based on the usual analysis, the pore diameter can be related to the local stress through the relation

$$\sigma > \frac{n\gamma}{r} \quad (7)$$

where γ is the interfacial energy and r is the pore radius. The value of n in the case of a cylindrical pore at a triple junction may be taken as 0.5-0.7 depending on the contact angle. The stress is therefore determined to be on the order of $\sim 1 \text{ GPa}$ or $\sim 10^2 G$, where G is the shear modulus. Although this is well beyond the yield point of 'normal' Au or Ag, no dislocation-based plasticity was observed in the experiments described in Section 2.2. The individual crystals in the nanograin material appear to have a significantly higher yield point than the corresponding normal grain size material. It is proposed here that this is related to the lack of dislocations, and thus the lack of dislocation sources, in the interior of nanocrystalline grains. This points to an analogy with the mechanical behavior of a defect-free whisker. It should not be surprising that the behavior of a grain in the nanocrystalline material has a high yield point for dislocation-based plasticity if dislocation production is difficult.

As previously noted, no dislocations were observed in the interior of the grains in the 10 nm grain size material. A possible explanation of this observation and the resulting implications

for the mechanical behavior of the nanocrystalline material is the image forces on dislocations due to the close proximity of grain boundaries. Attractive forces between dislocations and grain boundaries arise because there are no long range stresses associated with the low energy dislocation structure at a grain boundary. The elastic energy of a dislocation is therefore less in the organization of a grain boundary structure than a dislocation isolated in the grain interior [22]. As a result, there will be a reduction in energy as the dislocation approaches the grain boundary, provided there is sufficient thermal energy to allow for rearrangement of the grain boundary structure. This type of thermal energy is likely present during the deposition process. The strain energy of a dislocation can be written in a general form applicable to the two limiting cases to be considered in this model

$$\frac{\text{energy}}{\text{length}} = \frac{Gb^2}{4\pi} \ln\left(\frac{x+D/2}{b}\right) \quad (8)$$

Equation 8 is applicable when $x \gg D$ and when $x=0$, where x is the distance from grain boundary and D is the spacing of dislocations in the grain boundary. For these two limiting cases, Equation 8 reverts to the relevant expressions in [22]. The magnitude of the image force per unit length is determined by the derivative of Equation 8 with respect to x . The image force per unit length (τb) acting to move a dislocation in the center of a grain of diameter d to the grain boundary is thus determined as the derivative of Equation 2 evaluated at $x=d/2 \gg D$, or

$$\tau b \approx \frac{Gb^2}{2\pi d} \quad (9)$$

where τ is the image stress. For a dislocation to be stable in the vicinity of the grain boundary during processing, the image stress must be less than the stress necessary to move dislocations from their original (grown in) positions. It is not straightforward to determine this stress. In the case of glissile dislocations on the {111} glide planes, and ignoring pinning effects of the grain boundaries on the "ends" of the dislocations as well as line tension forces (as the dislocation bows towards the grain boundary) and solute strengthening, this resisting stress would be the {111}<110> CRSS of pure gold, about 1-3 MPa depending on the purity. However, grown-in dislocations often thread crystals on planes other than the glide planes, and so the resisting stress may be dominated by the CRSS on non-glide planes. Further, thin film deposition is an energetic process, and so climb may be important. As a first approximation, we assume here that the resisting stress is about equal to the "yield stress" of commercial purity gold or silver, about 35 MPa. For $d=10$ nm, the image stress is on the order of $4 \times 10^{-3} G$ or around 300 MPa. This is substantially greater than the yield point of normal Au or Ag (~35 MPa). This suggests that any dislocations which might be present in the grain interior during processing when the material is 'hot' would be forced to the grain boundary, resulting in dislocation free nanocrystallites. However, if the 100 nm grains are considered, Equation 9 determines an image stress on a dislocation at the grain center which is less than the yield stress. This suggests that the dislocations are stable at the grain center and may act as sources for dislocation reproduction.

The image force approach can be extended to consider the stress required to activate a grain boundary source by evaluating the derivative of Equation 8 with respect to x at $x=0$ and assuming that $D=b$. This approximates the stress required to pull a grain boundary dislocation into the grain interior as

$$\tau_{gb} \approx \frac{G}{2\pi} \approx 12 GPa \quad (10)$$

This appears to be well above the stress determined by the pore diameter measurements. In fact, at low strain rates grain boundary sliding may act to keep the stress lower than τ_{gb} . Application of the Mukherjee model [23] of grain boundary sliding controlled plasticity to our case where $d=10$ nm, the strain rate is 10^{-4} /s, and the grain boundary diffusion coefficient is 10^{-15} cm²/s gives a stress which is consistent with the pore diameter measurement. For this diffusion coefficient, the Mukherjee model has the form for Au/Ag

$$\dot{\epsilon} \approx \frac{10^4}{s} \left(\frac{b}{d} \right)^2 \left(\frac{\sigma}{G} \right)^2 \quad (11)$$

Using Equations 10 and 11, it is possible to determine a critical strain rate at which dislocation based plasticity due to grain boundary sources might occur. In other words, when the stress in Equation 11 approaches the value of τ_{gb} in Equation 10, grain boundary sources may become active. Carrying out this algebraic manipulation determines the critical strain rate at

$$\dot{\epsilon}_{critical} \approx \frac{10^4}{s} \left(\frac{b}{d} \right)^2 \frac{1}{4\pi^2} \quad (12)$$

Equation 12 agrees with the experimental observations in that the strain rate present in our experiments (10^{-4} /s) is too low to observe grain boundary dislocation sources in the 10 nm material. But this strain rate is also just below what is required to observe active grain boundary dislocation sources in the 100 nm grain size material. However, dislocation sources may be present in the interiors of these larger grains. Another limiting factor as to the operation of grain boundary sources is the consideration that the large stresses required to activate dislocation sources in the 10 nm grains will not occur at the head of a pile-up, for there are no dislocations in the grain interior. In this case, dislocation structures cannot induce a line source of stress at the grain boundary. Instead, the stress will be applied more uniformly to the grain boundary. This may cause a loss of cohesion at the grain boundary and failure by brittle fracture before the activation of grain boundary sources.

4.3 A Gradient Elasticity Model for Nanostructured Materials [17]

As before, assume that the nanostructured material consists of two states, a boundary state and a bulk state. Since the grain size is very small, assume that the two states occupy the same material point. The two states can interact mechanically via an internal body force vector \hat{f} which enters into the momentum balance equation for each state (grain space is indicated by index 1 and grain boundary space is indicated by index 2) as follows

$$\operatorname{div}\underline{\sigma}_1 = \hat{f}, \quad \operatorname{div}\underline{\sigma}_2 = -\hat{f}; \quad \operatorname{div}\underline{\sigma} = 0 \quad (13)$$

where $\underline{\sigma}_{1,2}$ denotes the partial stresses of the two superimposed states and $\underline{\sigma} = \underline{\sigma}_1 + \underline{\sigma}_2$ denotes the total stress.

By assuming that each state (or phase) obeys Hooke's law and that the interaction force is proportional to the difference of the individual displacements, we have

$$\begin{aligned} \underline{\sigma}_k &= L_k \underline{u}_k, \quad k = 1, 2; \quad \hat{f} = \alpha(\underline{u}_1 - \underline{u}_2) \\ L_k &= \lambda_k G + \mu_k \hat{\nabla}; \quad G = I \operatorname{div}; \quad \hat{\nabla} = \nabla + \nabla^T \end{aligned} \quad (14)$$

where α is a constant and the Lamé constants (λ_k, μ_k) have their usual meanings. It turns out that uncoupling of Equations 13 and 14 by the methods described in [17,24] results in the differential equation

$$\mu \nabla^2 \underline{u} + (\lambda + \mu) \operatorname{div} \underline{u} - c \nabla^2 [\mu \nabla^2 \underline{u} + (\lambda + \mu) \nabla \operatorname{div} \underline{u}] = 0 \quad (15)$$

where \underline{u} is the total displacement of the nanostructured material. [The total displacement is defined as a linear combination of \underline{u}_1 and \underline{u}_2 which may properly consider the volume fraction of each phase.] In deriving Equation 15, it was assumed that the two phases share the same shear modulus; otherwise two constants occur in the higher order gradient part of Equation 15. Also, the constants λ and μ relate explicitly to those appearing in Equation 14. The system of the above differential equations may suggest that the static elastic deformation of a nanostructured material could be described by the equilibrium equations, Equation 13, for the total stress $\underline{\sigma}$ with the following gradient modification of Hooke's law

$$\underline{\sigma} = \lambda(\operatorname{tr} \underline{\varepsilon}) I + 2\mu \underline{\varepsilon} - c \nabla^2 (\lambda(\operatorname{tr} \underline{\varepsilon}) I + 2\mu \underline{\varepsilon}) \quad (16)$$

where $\underline{\varepsilon}$ is the total strain given in terms of displacement by the usual relation $\underline{\varepsilon} = (\hat{\nabla} \underline{u})/2$. The constitutive Equation 16 is a special form of the gradient elasticity theory which has been adopted to discuss the structure of the crack tip (see, for example, [24]). The coefficient c may be positive or negative. Positive values of c ensure global uniqueness of boundary value problems, while negative values of c ensure desirable dispersion properties of the corresponding wave propagation

problem. It turns out that adoption of Equation 16 to solve crack problems eliminates the strain singularity at the crack tip and substantiates the “cohesive zone” hypothesis of Barenblatt [25], which should be quite relevant at small material scales. Moreover, for negative values of c (when uniqueness of boundary value problems is not ensured), it can be shown that Equation 16 leads to undulated crack profiles like those depicted in Figure 5, observed in nanostructured films just before crack bifurcation occurs. In this connection, it is pointed out that the wavelength of the observed crack undulations is about ten times larger than the grain size. Simple dimensional arguments suggest that the gradient coefficient c is proportional to the square of an internal length scale, l . While in the case of traditional materials, l may be associated with the grain size, in the present case of nanostructured materials it is possible that the important length scale in the crack propagation process is related to *groups* of grains, deforming in a cooperative fashion, as has been observed in the grain rotation experiments similar to those shown in Figure 7. Further work in this area is in progress.

4.4 A Simple 1-D Plasticity Model for Nanostructured Materials [26]

Based on the experimental observations reported above, a simple plasticity model for nanocrystalline metals has been developed. It assumes that the strain rate has three components, caused respectively by diffusional flow, grain boundary deformation, and pore growth. Therefore, in one dimension,

$$\dot{\epsilon} = \dot{\epsilon}_1 + \dot{\epsilon}_2 + \dot{\epsilon}_{12} \quad (17)$$

where $\dot{\epsilon}_1$ is associated with diffusion, $\dot{\epsilon}_2$ is associated with dislocation climb and possibly glide in the grain boundaries, and $\dot{\epsilon}_{12}$ is associated with cavity nucleation, growth and migration. Next, physically-based constitutive equations for the various strain rate components are adopted by involving arguments previously developed for related deformation mechanisms in superplasticity. We confine attention to cases where elastic deformation is negligible, the local stress is adequately represented by the applied stress, and grain boundary sliding and rotation are accommodated by vacancy diffusion in both the bulk and grain boundary space, as well as by climb of grain boundary dislocations. Then, the following expressions can be written for $\dot{\epsilon}_1$ and $\dot{\epsilon}_2$ (see, for example, [27] for a review of related mechanisms for superplastic flow)

$$\dot{\epsilon}_1 = K_1 \left(\frac{b}{d} \right)^2 D_{eff} \left(\frac{\sigma}{E} \right) \quad (18)$$

$$\dot{\epsilon}_2 = K_2 \left(\frac{b}{d} \right)^2 D_B \left(\frac{\sigma}{E} \right)^2 \quad (19)$$

where K_i are constants, b is the Burgers vector, d is the grain size, σ and E are the applied stress and Young's modulus, D_B is the grain boundary diffusivity, and the effective diffusivity, D_{eff} , is given by

$$D_{eff} = D_L \left(1 + \frac{3.3\delta}{d} \frac{D_B}{D_L} \right) \quad (20)$$

where D_L denotes the lattice diffusivity, and δ is the grain boundary thickness.

Both $\dot{\epsilon}_1$ and $\dot{\epsilon}_2$ would contribute to a decreasing flow stress with decreasing grain size, which has not been observed in metals at room temperature, as discussed in Section 4.1. However, as predicted by the model developed in Section 4.1, this type of behavior is not expected in metals at room temperature until the grain size is reduced below about 5 nm, and to date no metals have been produced with this small of a grain size. Further, with slightly increasing temperature, the grain size at the peak strength would be expected to increase. Therefore, this type of model would be expected to be useful either in metals with grain sizes below 5 nm, or in coarser structures at slightly elevated temperatures.

It is not straightforward to write down an evolution equation for $\dot{\epsilon}_{12}$ by resorting to superplasticity arguments. One may do so, however, for the nanoporosity

$$\varphi = \zeta n r^3 \quad (21)$$

where ζ is a numerical factor ($\zeta = 4\pi/3$ for spherical voids), n is the number of voids per unit volume, and r is the average pore radius. In cavitation damage theories, evolution equations for the nucleation rate \dot{n} and \dot{r} are provided (see, for example [28,29] and references quoted therein). Then, the evolution of φ can be computed from the kinematic relation

$$\dot{\varphi} = \varphi \left(\frac{\dot{n}}{n} + 3 \frac{\dot{r}}{r} \right) \quad (22)$$

along with appropriate equations for \dot{n} and \dot{r} , which are available from cavitation studies. These evolution equations, along with Equations 21-22, can provide the desired equation for $\dot{\epsilon}_{12}$ by assuming that this is proportional to the nanoporosity, *i.e.*

$$\dot{\epsilon}_{12} = \Lambda \dot{\varphi} \quad (23)$$

This completes the set of equations which could be viewed as a basis for developing a three-dimensional flow theory for nanostructured materials.

4.5 A 3-D Phenomenological Plasticity Model for Nanostructured Materials [30]

Motivated by the one-dimensional microscopic arguments presented above, one may propose, in three dimensions, a linear dependence of the strain rate tensor $\dot{\epsilon}_1$ on the stress tensor σ and a quadratic dependence of the strain rate deviator $\dot{\epsilon}'_2$ on the effective (or Mises) stress,

$$\tau = |\underline{\sigma}'| = \sqrt{\frac{(\underline{\sigma}' \cdot \underline{\sigma}')}{2}} \quad (24)$$

as follows

$$\dot{\underline{\epsilon}}_1 = A\underline{\sigma} ; \quad \dot{\underline{\epsilon}}_2 = B\tau^2 \frac{\underline{\sigma}'}{2|\underline{\sigma}'|} \quad (25)$$

The prime denotes the deviatoric part and the orientation quantity $\underline{\sigma}'/2|\underline{\sigma}'|$ simply indicates that the (eigen) directions of $\dot{\underline{\epsilon}}_2$ are determined by the principal directions of the applied stress. The phenomenological coefficients A and B may depend on the stress invariants $\sigma_h = (\text{tr}(\underline{\sigma}))/3$ and τ but, in a first step, they may be assumed constants depending on the grain size, diffusivities and temperature. Moreover, $\dot{\underline{\epsilon}}_1$ may be assumed as having only a hydrostatic component, while $\dot{\underline{\epsilon}}_2$ has only a deviatoric part. More experiments and microscopic arguments are required to further justify or modify the above assumptions. The final point we wish to address here is the inelastic strain rate $\dot{\underline{\epsilon}}_{12}$ due to nanopore development. In a first approximation this component is assumed to be hydrostatic and proportional to the rate of (nano)porosity $\dot{\phi}$. The nanoporosity ϕ is assumed to obey a complete balance law containing a flux term associated with the migration of nanopores and a source term associated with the growth and coalescence of nanopores. In view of these arguments we can write

$$\dot{\underline{\epsilon}}_{12} = \Lambda \dot{\phi} \underline{I}; \quad \dot{\phi} + \text{div} \underline{j} = \hat{c} \quad (26)$$

where Λ is a phenomenological coefficient, \underline{j} is the flux and \hat{c} is the source or production term modeling nanopore growth and coalescence. The term \hat{c} depends, in general, on the stress invariants σ_h and τ , while the flux \underline{j} may be taken proportional to the gradients of τ and σ_h , i.e.

$$\hat{c} = \hat{c}(\tau, \sigma_h); \quad \underline{j} = -D \nabla \tau + M \nabla \sigma_h \quad (27)$$

where D and M are phenomenological coefficients. The first term on the right hand side of the expression for \underline{j} in Eq. 27 denotes the flux induced by the gradient of the (nano)slip, while the second term denotes the flux induced by the gradient of the hydrostatic stress. The specific dependence of \hat{c} on τ and σ_h may also be motivated by the microscopic arguments contained in Equations 21-23, and, in a first approximation, \hat{c} may be taken to be linear in σ_h and quadratic in τ . The combination of Equations 25-27 results in a stress-gradient expression for the total inelastic strain rate $\dot{\underline{\epsilon}} = \dot{\underline{\epsilon}}_1 + \dot{\underline{\epsilon}}_2 + \dot{\underline{\epsilon}}_{12}$.

5. MODELING OF MATERIAL INSTABILITIES AND STRAIN GRADIENT EFFECTS

This has been a prolific area of research. The AFOSR support has been essential in integrating and further developing our earlier ideas (since 1984) on material instabilities and gradient effects. While these ideas were reluctantly received at the beginning by the physics, materials and mechanics communities, it is clear now that they have made a definite impact, as more and more research groups in the U.S. and abroad are rapidly turning their attention to them. Two particular thrust areas are leading the way: (i) dislocation patterning and (ii) gradient plasticity, with two secondary research areas following: (iii) gradient elastic fracture mechanics and (iv) oscillatory fracture. A summary of some basic results from this research is given below.

5.1 Dislocation Patterning

This important problem of material stability and structure formation at the dislocation level has currently received substantial attention by the materials, physics and mechanics communities from both theoretical and numerical points of view. The need for addressing this problem was recognized at MTU more than a decade ago and more results have been obtained recently by our group.

The basis for analyzing dislocation patterns is the following reaction-diffusion equations for defect densities ψ_i (with v_i denoting the corresponding defect velocities)

$$\frac{\partial \psi_i}{\partial t} + \operatorname{div}(\psi_i v_i) = g_i(\psi_j) + D_i \nabla^2 \psi_i \quad (28)$$

Here $g(\psi_i)$ are nonlinear functions of defect densities (collision integrals) describing defect generation, multiplication and annihilation, as well as reactions between defects of different types. The divergence term models the defect transport due to long-range interactions and external factors. The diffusion term is, in principle, of stochastic nature, but it can also be derived from the divergence term as was illustrated by the Aifantis (see references quoted in [31]) and discussed by Romanov and Aifantis [32-34].

Romanov and Aifantis [32-34], in particular, proposed a three-element kinetics model by identifying $\psi_1 = \rho$ (density of fast moving mobile dislocations), $\psi_2 = \varphi$ (density of slow moving dislocation dipoles), and $\psi_3 = \theta$ (density of disclination defects or immobile dislocations in terminated walls). Then by combining the drift and diffusion terms in Equation 28 into an effective diffusion-like term, and assuming specific forms for $g(\psi_i)$ dictated by the defect

reactions, they applied the three-element defect kinetics model to various physical situations. This approach was motivated by the reaction-diffusion scheme adopted earlier by Walgraef and Aifantis (see, for example, references quoted in [31]) which, in turn, was an outgrowth of the earlier gradient-dependent dislocation kinetics models proposed by Aifantis in 1983 (see reference quoted in [31]).

$$\begin{aligned}\frac{\partial \rho}{\partial t} &= F(\rho) - h(\vartheta)B\rho^2 + \gamma C\rho\vartheta + \eta N\vartheta\varphi + D_\rho \frac{\partial^2 \rho}{\partial x^2} \\ \frac{\partial \varphi}{\partial t} &= -K(\varphi) + \beta h(\vartheta)B\rho^2 - C\rho\varphi + N\vartheta\varphi + D_\varphi \frac{\partial^2 \varphi}{\partial x^2} \\ \frac{\partial \vartheta}{\partial t} &= -G(\vartheta) + \mu M\rho\vartheta\end{aligned}\quad (29)$$

Here B, C, M, N, K are constants characterizing reactions between defects. For example, C characterizes the collision of a dislocation with a dipole which results in dipole disappearance and production of new mobile dislocations. The coefficient $\gamma (0 < \gamma < 2)$ indicates that, as a result of this reaction, we may have either dipole annihilation or disassociation. Similar meaning is attributed to the coefficients (β, μ, η), while the function $h(\varphi)$ describes the possible catalytic role of disclination defects in the process of dislocation annihilation. Finally, functions $F(\rho)$, $K(\vartheta)$ and $G(\vartheta)$ are responsible for the production/disappearance of a given type of the defect in the absence of others.

The main property of the system (29) for the dislocation-dislocation dipole-disclinations kinetics is the existence of multiple steady-state solutions, depending on the values of the model parameters. Transitions from one state to another are associated with instabilities occurring during the process of plastic deformation. For example, two stationary solutions are possible for dislocation - dipole kinetics ($\vartheta = 0$) only if the product $\beta\gamma$ connected with the rates of production and destruction of dipoles) is large enough ($\beta\gamma > 1$). For typical values of the parameters involved, the above kinetic system permits stationary space periodic solutions which may be related with dislocation and disclination structures in deformed crystals.

5.1.1 Dislocation Patterning in Crack Tips [33]

In the case of defect kinetics in front of a growing crack, our model involves gliding dislocations in the plastic zone $\psi_1 = \rho$, low-mobility dislocation dipoles $\psi_2 = \varphi$, and immobile crack dislocations $\psi_3 = \xi$. The appropriate system of reaction-diffusion equations reads

$$\begin{aligned}
 \frac{\partial \rho}{\partial t} &= A\xi - B\rho^2 + \gamma C\rho\varphi - E\rho + D_\rho \frac{\partial^2 \rho}{\partial x^2} \\
 \frac{\partial \varphi}{\partial t} &= \beta B\rho^2 - C\xi\varphi - K\varphi + D_\varphi \frac{\partial^2 \varphi}{\partial x^2} \\
 \frac{\partial \xi}{\partial t} &= E\rho - F_\xi(\xi)
 \end{aligned} \tag{30}$$

where $A, B, C, E, K, F, \gamma, \beta$ are constants, similar to those introduced in (29), and $F_\xi(\xi)$ is a function describing the emergence of microcracks with the macrocrack. The one-dimensional character of the model follows from the assumption that the thickness of the plastic zone is much smaller than its length.

Linear stability analysis of system (30) shows the occurrence of spatially periodic solutions. For reasonable values of the material coefficients, it turns out that the corresponding wavelength is of the order of $1-10h$ where h is the plastic zone height.

Thus, the analysis of the simultaneous development of (plastic) deformation and (micro) fracture events ahead of the crack tip demonstrates the possibility of nonuniform distributions of the (micro) crack dislocation density ξ . In particular, it may be shown that oscillations in the crack opening displacement are in phase with nonuniformities of the low-mobility dislocation (dislocation dipoles φ) distribution.

The physical configuration to which Equations 30 apply and the results of the analysis of these equations are shown in Figures 21 and 22 respectively, while Figure 23 shows schematically the implications of the analysis in obtaining periodic solutions for the crack tip opening displacement in ductile fracture.

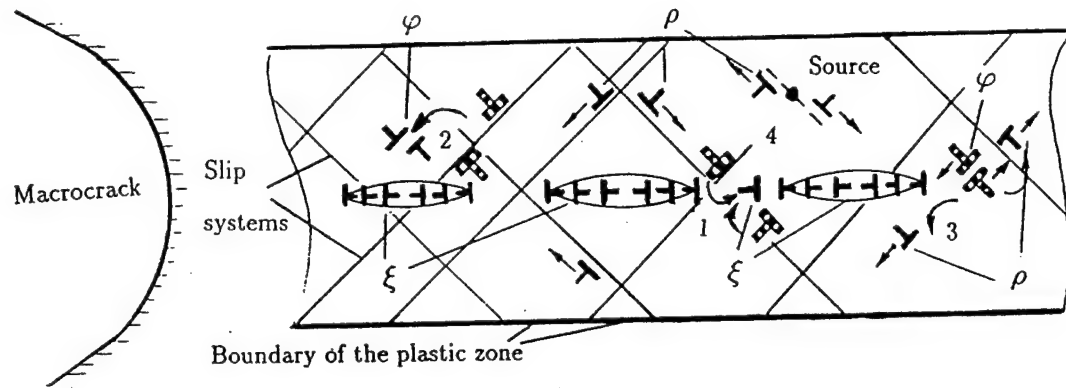


Figure 21 Three-element dislocation kinetics model in the plastic zone of a crack, where ρ is the dislocation density, φ is the dislocation dipole density, and ξ is the microcrack dislocation density.

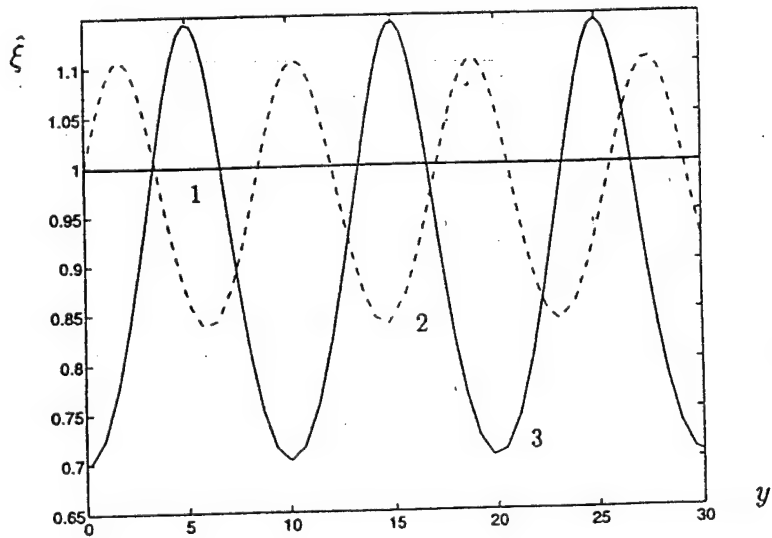


Figure 22 Stationary distributions for the relative density of microcrack dislocation ξ as a function of the space coordinate y . (1) uniform solution; (2), (3) nonuniform oscillating solutions for different boundary values of ξ and $\xi' = d\xi/dy$ at $y = 0$.

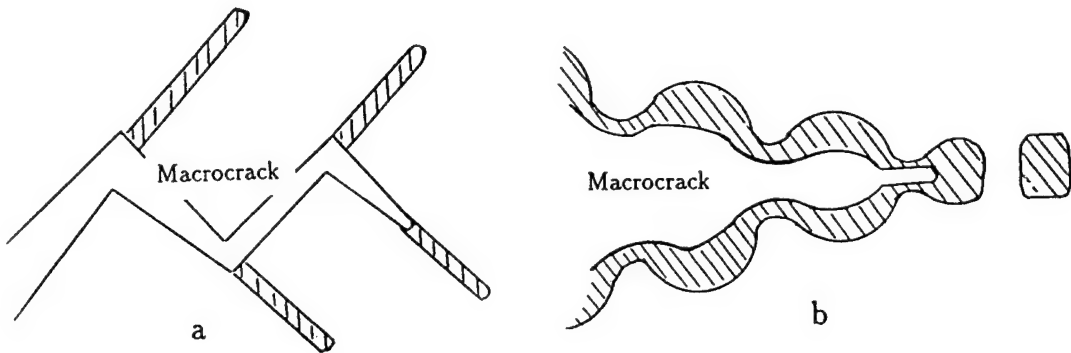


Figure 23 Discontinuous subcritical crack growth due to instabilities in the plastic zone ahead of the crack tip.

5.1.2 Dislocation Patterning in Thin Films [34]

It is well-known that during epitaxial growth of thin films on solid substrates, a mechanism of coherency breaking is the creation of misfit dislocations which appear at the interface as a result of the need to relax the stress caused by the misfit. The standard approach used for the interpretation of the commonly observed distribution of equally spaced misfit dislocations is based on the minimization of strain energy. This approach gives, among other things, a critical film thickness characterizing the appearance of misfit dislocations of uniform density $\psi_o = f/b$ where b is the Burgers vector and $f = (\alpha_s - \alpha_o)/\alpha_o$ is the misfit strain with (α_s, α_o) denoting respectively the lattice parameters of the substrate and the film. The resulting misfit elastic stress is $\sigma_f = cf$ where $c = E/(1 - \nu^2)$ with E denoting the Young's modulus and ν the Poisson's ratio. The misfit dislocations exert a back stress σ_ψ which may be assumed to depend linearly upon the density ψ and its spatial gradients up to the fourth order. Thus, the total stress field $\sigma = \sigma_f + \sigma_\psi$ on the film can be written as

$$\sigma = c(f - b\psi) - \bar{c} \frac{\partial^2 \psi}{\partial x^2} - \bar{\bar{c}} \frac{\partial^4 \psi}{\partial x^4} \quad (31)$$

where the gradient coefficients \bar{c} and $\bar{\bar{c}}$ are assumed to be constants.

The total stress field σ in the film acts upon mobile dislocations of density ρ nucleated from sources at the top free surface to be subsequently directed towards the film/substrate interface by gliding along conjugate slip planes. During this process, the ρ -dislocations may interact with each other when they meet at the intersections of glide planes to form sessile dislocations of density φ with Burgers vector parallel to the interface, where formation of misfit dislocations of density ψ takes place. A schematic of this three-element defect kinetics model as applied to thin films is shown in Figure 24.

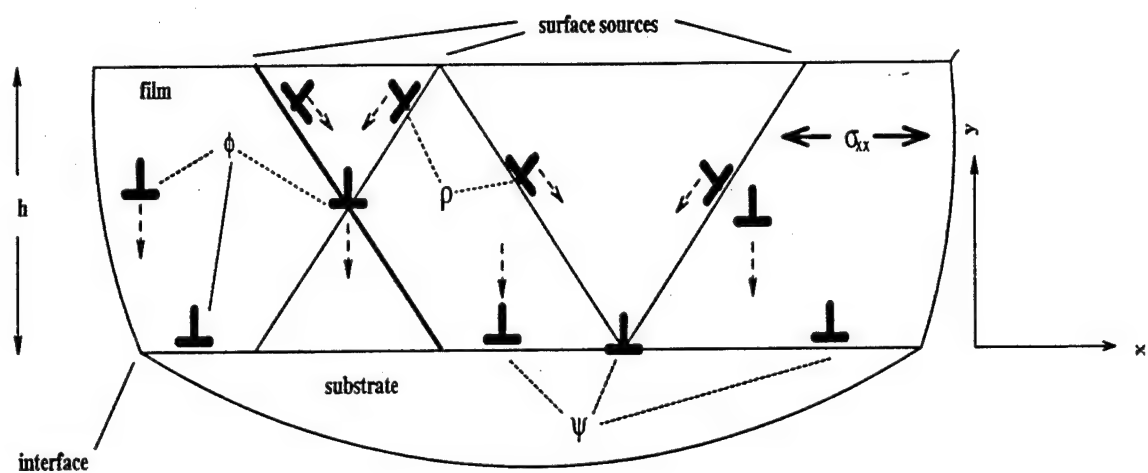


Figure 24 Three-element reaction-diffusion model for defect kinetics in thin films. Here σ_{xx} is the tensile misfit strain in the film ($\sigma_{xx} \approx Ef$, where E is the elastic modulus and f is the misfit strain); ρ is the density of mobile (gliding) dislocations; φ is the density of slow mobile (climbing) dislocations; and ψ is the linear density of misfit dislocations.

The transport-reaction processes between the aforementioned types of linear defects can be expressed as follows

$$\begin{aligned}
 \frac{\partial \rho}{\partial t} &= A\sigma - B\rho + D \frac{\partial^2 \rho}{\partial x^2} \\
 \frac{\partial \varphi}{\partial t} &= B\rho - K\varphi \\
 \frac{\partial \psi}{\partial t} &= Kh\varphi
 \end{aligned} \tag{32}$$

where the various coefficients are taken as constants and h denotes film thickness. Upon combination of (31) and (32) the following dimensionless form of coupled diffusion-reaction equations is obtained

$$\begin{aligned}\frac{\partial \rho}{\partial t} &= c_1 \left(1 - \psi - c_3 \frac{\partial^4 \psi}{\partial x^4} \right) - c_2 \rho + \frac{\partial^2 \rho}{\partial x^2} \\ \frac{\partial \varphi}{\partial t} &= c_2 \rho - \varphi \\ \frac{\partial \psi}{\partial t} &= \varphi\end{aligned}\tag{33}$$

where the new variables are properly normalized and the new constants are directly related to those appearing in (32).

A uniform steady solution of (33) is $(1, 0, 0)$ and it corresponds to the equilibrium state of equally spaced misfit dislocations. [Note that the value of 1 obtained for ψ is due to the fact that ψ in (33) is normalized with $\psi_0 = f/b$ in (32)]. In examining the linear stability analysis of (33), $[(\rho, \varphi, \psi) \sim \exp(iqx + \omega t); q = \text{wavelength}, \omega = \text{growth rate}]$ we find the following dispersion equation

$$\omega^3 + (1 + c_2 + q^2)\omega^2 + (c_2 + q^2)\omega + c_1 c_2 (1 - c_3 q^2 + c_4 q^4) = 0\tag{34}$$

A "turing instability" leading to a spatially periodic pattern with a preferred wavelength occurs when

$$\omega(q) > 0 \quad \text{and} \quad \left. \frac{\partial \omega(q)}{\partial q} \right|_{q=q_{pref}} = 0\tag{35}$$

and, in view of (35), it turns out that this is possible when

$$c_3 \geq 2\sqrt{c_4}, \quad \text{with} \quad c_1 < (1/c_2 c_4)\tag{36}$$

In this connection, it is also interesting to note that it is possible to find exact stationary solutions of the system of Equations (33) by setting the time derivatives equal to zero. Then ρ and φ vanish, while the normalized misfit dislocation density ψ is given by the equation

$$\psi = 1 + \sum_{i=1}^4 C_i \exp[\pm x(-c_3 \pm \sqrt{a})/2c_4]^{1/2}\tag{37}$$

with $a = c_3^2 - 4c_4$ and C_i 's constants of integration. The above solution is periodic when the

following condition holds

$$c_3^2 > 4c_4 > 0 \quad (38)$$

a fact consistent with the linear instability analysis, as suggested by (36)₁.

Preliminary estimates for the phenomenological coefficients indicate that the aforementioned “turing instability” but also other more complex types of spatio-temporal instabilities are possible when the value of the film thickness exceeds a critical one ($h > h_{cr}$). These findings are in qualitative agreement with experimental observations where, when the film thickness exceeds a certain value, a symmetry breaking mechanism occurs and the uniform equilibrium distribution of equally spaced misfit dislocations becomes unstable in favor of spatio-temporal patterns.

5.2 Gradient Plasticity

The various successes of this theory, also introduced a decade ago at MTU by essentially incorporating the Laplacian of effective plastic strain into the yield condition, are outlined in [31]. Among them, we distinguish the determination of shear band widths and spacings, as well as the settlement of convergence and mesh-size in dependence of finite element analyses in the material strain softening regime. All these features cannot be captured by classical theories of plasticity or viscoplasticity which do not incorporate a internal length scale into the constitutive equation. New insights into the gradient plasticity theory were gained in the course of the present work, especially in relation to estimates pertaining to the gradient coefficients prediction of size effects and conclusions about adiabatic shear banding.

5.2.1 Estimates for the Gradient Coefficients

The original form of gradient plasticity theory developed at MTU is based on the following gradient-dependent modification of the “homogeneous” plastic flow expression $\tau = \kappa(\gamma)$

$$\tau = \kappa(\gamma) - c\nabla^2\gamma - \bar{c}|\nabla\gamma|^2 \quad (39)$$

where (τ, γ) denote respectively the equivalent (or effective) stress and plastic strain, and (c, \bar{c}) are the so-called gradient coefficients. Estimates for the coefficient c (as well as for the coefficient \bar{c}) were obtained recently by using a self-consistent scheme for plastic polycrystals. In general, these estimates give

$$|c| = CR^2 \quad (40)$$

where C is a material constant related in a specific way to the shear modulus (μ) Poisson’s ratio

(v), and tangent modulus (h) and $R = d/2$ where d denotes the average grain size. [Relevant expressions for C are given in [31] and typical values of c are given in the Table below].

Table 2: Estimates for the gradient coefficient, c , for $10 \mu\text{m} \leq R \leq 100 \mu\text{m}$, $h \approx 0$.

Material	μ (GPa)	v	$ c $ (N) (KBW)	$ c $ (N) (Lin)
Structural Steel	70-80	0.33	0.373-37.26	0.7-80
Copper & its alloy	40-60	0.33-0.35	0.213-32.31	0.4-60
Aluminum & its alloys	26-30	0.31-0.34	0.137-16.06	0.26-30

5.2.2 Size Effects

In discussing the ability of our gradient approach to capture size effects, it is worth mentioning that a different strain gradient plasticity theory has recently been proposed by Fleck, Muller, Hutchinson and Ashby (see reference quoted in [31]). Their theory is based on the Cosserat approach using an asymmetric stress, it is physically justified through Ashby's concept of "necessary geometric dislocations" and experimentally motivated by size effects in plastic torsion of thin Cu wires where the stress-strain response is found to depend on the wire radius. A brief but critical discussion of this theory is given in [31] where a comparison with the original theory based on Equation 31 is given. In this discussion it is also emphasized that the theory of Equation 31 can predict the "size effect" quoted by Fleck, Muller, Hutchinson and Ashby in a quantitative (rather than a qualitative) way. The result of this prediction is shown in Figure 25. The two plots correspond to torque (Q) - surface strain (γ_s) data for two wires of radii $a = 85 \mu\text{m}$ and $a = 15 \mu\text{m}$ respectively. The theory of Equation 31 results in the relation

$$Q = 2\pi \left(\kappa_o a^3 \frac{\gamma_s^n}{3+n} - ca \frac{\gamma_s}{2} - \bar{c} a \frac{\gamma_s^2}{3} \right) \quad (41)$$

where (κ_o, n) denote the hardening parameters in the homogeneous flow stress expression $\kappa = \kappa(\gamma) = \kappa_o \gamma^n$, ($\kappa_o = 117 \text{ MPa}$, $n = 0.2$), and the gradient coefficients take the values $c = -0.01 \text{ N}$, $\bar{c} = 0.006$. On the other hand, the self-consistent estimate gives an absolute value for the coefficient c in the range of $0.013\text{N} - 0.505\text{N}$ for a grain size in the range $5 - 25 \mu\text{m}$.

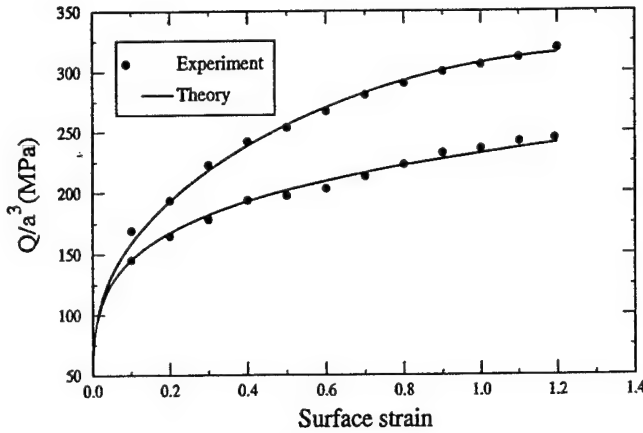


Figure 25 Torque - surface strain plots for two different diameters of fine wire.

5.2.3 Adiabatic shear banding [35]

The initiation of adiabatic shear banding has been a standard problem to consider within the solid mechanics literature dealing with the stability of deformation. Here the thermal conductivity in the energy equation provides an internal length scale which could serve, in principle, as a mechanism to capture the evolution of deformation in the softening regime. The basic equations used for the study of adiabatic shear banding in one dimension read

$$\tau_y = \rho v_t, \quad \rho c_v \theta_t = k \theta_{yy} + \tau \gamma_t, \quad \gamma_t = v_y \quad (42)$$

where the subscripts (t,y) denote respectively partial differentiation with respect to time and spatial coordinate normal to the plane of shear; (τ, γ) denote the shear stress and strain; (ρ, c_v, k) denote mass density, specific heat and thermal conductivity, respectively; while v is the velocity and θ is the temperature. Equation $(42)_1$ is the balance of linear momentum, $(42)_2$ is results from the balance of internal energy, and $(42)_3$ is a compatibility condition. The one-dimensional shear stress τ , which here coincides with the equivalent three-dimensional shear or flow stress, is given by a yield or flow condition of the form

$$\tau = \kappa(\gamma, \gamma_t, \theta) - c \nabla^2 \gamma \quad (43)$$

where $\kappa(\gamma, \dot{\gamma}, \theta)$ denotes the homogeneous part of the flow stress and $c\nabla^2\gamma$, with c denoting a phenomenological gradient coefficient, is an inhomogeneous contribution due to nonlocal hardening and heterogeneous deformation development. Standard adiabatic shear band analyses are based on the homogeneous part of flow stress only and disregard the effect of deformation heterogeneity accounted for by the Laplacian term.

By inspecting the system of Equations (42) and (43) and performing an approximate linear stability analysis, we can conclude that there are two competing internal length mechanisms: one associated with the strain gradient internal length l_c and another associated with the temperature gradient internal length l_k . They are given by the expressions [35]

$$l_c = \sqrt{-\frac{c}{H_c}} \quad ; \quad l_k = \sqrt{-\frac{ks}{\rho c_v H_c}} \quad (44)$$

where the newly appearing quantities s (>0) and H_c (<0) denote the strain rate sensitivity ($s \equiv \partial\kappa/\partial\dot{\gamma}$) and the critical value of the (total) hardening coefficient $H = d\tau/d\gamma = h + h_\theta$ with h being the strain hardening parameter ($h \equiv \partial\kappa/\partial\gamma > 0$) and h_θ the thermal softening parameter [$h_\theta \equiv (\tau/\rho c_v)(\partial\kappa/\partial\theta) < 0$]. Observations suggest that, in general, the sizes of adiabatic shear bandwidths scale with l_c rather than with l_k for typical values of the material parameters involved. Numerical analysis suggests that thermal conductivity alone (in the absence of gradient effects, $c = 0$) does not account for variations of shear bandwidths with varying the thermal length l_k and predicts, indeed, shear bandwidths smaller than the observed. Moreover, the mesh-size dependence and the associated “convergence” of the stress-strain graph in the softening regime is not decisively influenced by reasonable variations of the thermal conductivity length l_k . Both of these difficulties seems to be removed when the strain gradient internal length l_c is included, even in the case that thermal conductivity is neglected ($l_k = 0$).

Specifically, a complete linear stability analysis Equations 42 and 43 yields a cubic dispersion equation of the form

$$\omega^3 + A\omega^2 + B\omega + C = 0, \quad (45)$$

where the coefficients (A, B, C) are given explicitly in terms of the wave number of the fluctuation q , the quantities appearing in (44), and the values of stress and strain corresponding to the uniform solution which is used as a ground state for the perturbation technique. Instability occurs when a root of Equation 45 has a positive real part; a condition ensured by the Ruth-Hurwitz criterion

$$A \leq 0, \quad B \leq 0, \quad C \leq 0, \quad AB - C \leq 0. \quad (46)$$

It turns out that A is always positive, while the inequalities $B \leq 0$ or $C \leq 0$ predict a vanishing critical wave number (homogeneous oscillations). Thus, the only condition leading to spatio-temporal patterns is the last one in (46). In fact, by setting $\Phi \equiv \partial\kappa/\partial\theta$, we obtain the following

expressions for the critical hardening modulus H_c and the critical wave number q_c

$$H_c = -cq_c^2 + \frac{k[s(k + c_v s)q_c^4 + \Phi(\tau^o - s\gamma_t^o)q_c^2]}{-\rho c_v^2 s q_c^2 + \rho c_v^2 c} \quad (47)$$

$$q_c^2 = \frac{\Phi}{c_v s} \left[\gamma_t^o - \sqrt{\gamma_t^{o2} + \frac{\gamma_t^o c_v (\tau^o k - sk\gamma_t^o - \rho c_v \gamma_t^o)}{k^2 + kc_v s + \rho c_v^2 c}} \right]$$

The value of H_c predicted by (47)₁ is positive, indicating that deformation patterning initiates at the hardening regime. Moreover, for strictly adiabatic conditions ($k = 0$), a preferred wave number q_{pref} defined by the relation $\partial\omega/\partial q_{pref} = 0$ can be obtained. This is in contrast to the case where the gradient coefficient c is set identically equal to zero ($c \equiv 0$) giving an infinite wave number.

5.3 Gradient Elastic Fracture Mechanics [36-38]

The gradient plasticity theory discussed in the previous section is based on the introduction of an internal length scale in the expression for the flow stress as shown in Equations 39 or 43. An analogous internal length scale can be introduced within a purely elastic theory, by modifying the strain energy function. Within a nonlinear setting this was done by Trianfayllidis and Aifantis [37] to study localized shear zones in hyperelastic materials and, more recently, by Altan and Aifantis (as well as Ru and Aifantis [38], Unger and Aifantis [36]) within a linearized setting to study the structure of crack tip profiles. Within these latest works, it was shown that it is possible to eliminate the strain singularity that occurs at the crack tip. More importantly, it was shown that one can obtain oscillatory crack profiles [36], in agreement with the experimental observations in thin nanostructured films which are presented in Figure 5 of this report. The oscillatory crack profiles are shown in Figure 26 [36].

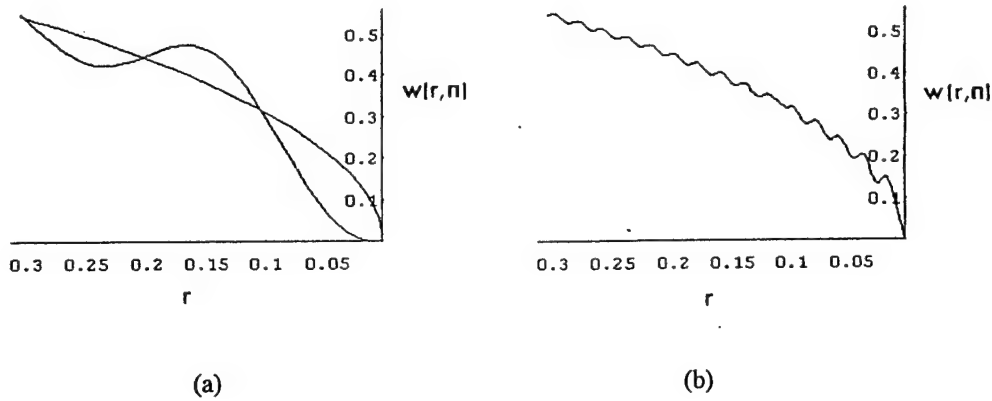


Figure 26 (a) Comparison of “gradient elastic” displacement for $c = -0.001$ along the crack axis (wavy curve) to the linear elastic displacement (parabolic curve) for Mode III cracks. (b) Mode III gradient elastic displacement along crack axis for $c = -1 \times 10^{-5}$.

The results of Figure 26 were obtained by using [36] the following stress-strain relations (for antiplane shear)

$$\sigma_{xz} = \mu \frac{\partial}{\partial x} (w - c \nabla^2 w), \quad \sigma_{yz} = \mu \frac{\partial}{\partial y} (w - c \nabla^2 w) \quad (48)$$

where μ is the shear modulus, w is the displacement and c is the gradient coefficient.

5.4 Oscillatory Fracture [39]

In this final section we consider spatio-temporal instabilities occurring during crack growth. Such instabilities are routinely observed in fracture tests of polymers under constant applied extension rate loading conditions. The phenomenon is commonly known as stick-slip fracture and manifests itself by oscillatory crack tip velocities and crack growth jumps. It is recorded as repeated cycles of fast unstable crack propagation and arrest resulting in periodic transverse arrest marks on the fracture surface and periodic load oscillations. A stick-slip fracture model is possible on the basis of a “non-monotonic” fracture toughness-velocity curve and an “inertia” modification of the energy balance equation dictating the motion of the crack. This modification reads

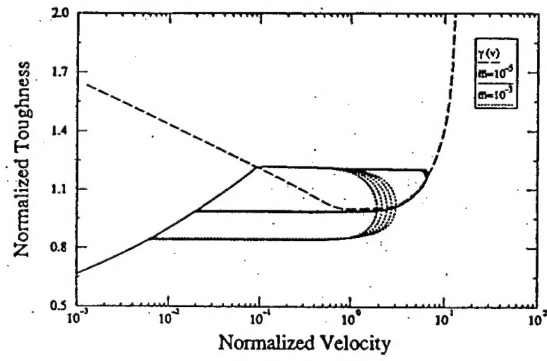
$$G_d = \gamma(v) + m v_t \quad (49)$$

where G_d denotes the dynamic energy release rate (expressed in terms of the applied load and crack characteristics); $\gamma(v)$ denotes fracture toughness (dependent on the surface energy and the energy dissipated during crack growth); and $m\dot{v}_t$ is a material inertia term (m denotes an effective mass and v denotes the crack velocity). When the function $\gamma(v)$ is monotonic, the crack velocity is continuous and no oscillations occur. When the function $\gamma(v)$ is non-monotonic and the loading conditions are such that the “imposed” crack velocity falls within the negative slope regime of the $\gamma - v$ graph, then a temporal instability takes place, oscillations in the crack velocity occur and a stair-case crack length vs. time profile is obtained.

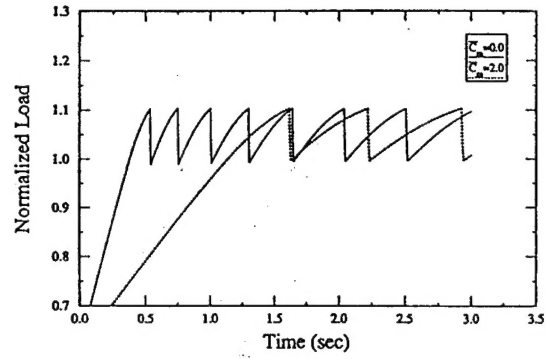
In fact, under certain approximations it is possible to cast (49) into the form

$$m\ddot{v}_t + \gamma'(v)\dot{v}_t + \kappa(v - V) = 0 \quad (50)$$

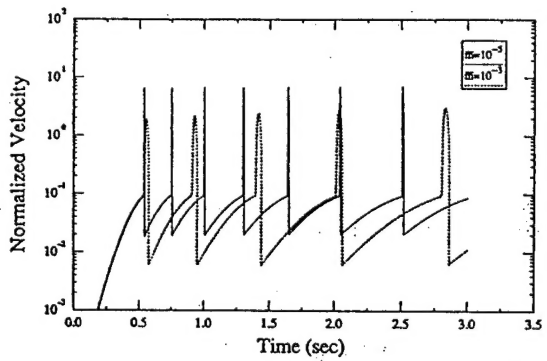
where (κ, V) are positive constants related explicitly to the loading conditions and geometry (load, displacement rate, initial crack geometry). The form of equation (50) is well-known in the theory of nonlinear dynamics. It is the Lienard's equations and it has appeared and analyzed before in the work of Aifantis and co-workers (see also [39] and references quoted therein) in relation to the problems of the Portevin-LeChatelier (PLC) effect and viscoelastic peeling. In the present case of stick-slip fracture it can be shown [39] that (50) leads to a limit cycle (relaxation oscillations) implying periodic velocity profiles, step-like crack growth, and load oscillations. These are shown in Figure 27 [39].



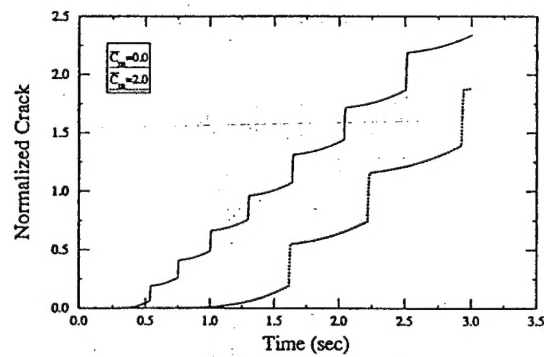
(a)



(b)



(c)



(d)

Figure 27 Periodic velocity profiles, step-wise crack propagation and load oscillations predicted by model. (a) The effect of crack tip inertia on limit cycles; (b) Sawtooth load profile showing the influence of loading machine compliance; (c) Crack tip velocity profile with respect to time showing the effect of crack tip inertia; (d) Step-like crack growth showing the influence of loading machine compliance.

6. REFERENCES

1. Siegel, R.W. (1993) *NanoStr. Mater.*, 3, 1-18.
2. Gleiter, H. (1989) *Prog. Mater. Sci.*, 33, 223-315.
3. Chokshi, A.H., Rosen, A., Karch, J., and Gleiter, H. (1989) *Scripta Metall.*, 23, 1679-1684.
4. Fougere, G.E., Weertman, J.R., Siegel, R.W. and Kim, S. (1992) *Scripta Metall. Mater.*, 26, 1879-1883.
5. Milligan, W.W., Hackney, S.A., Ke, M. and Aifantis, E.C. (1993) *NanoStr. Mater.*, 2, 267.
6. Ke, M., Hackney, S.A., Milligan, W.W. and Aifantis, E.C. (1995) *NanoStr. Mater.*, 5, 689-698.
7. Ke, M., Milligan, W.W., Hackney, S.A., and Aifantis, E.C. (1993) *MRS Proceedings*, 308, 565.
8. Milligan, W.W. and Hackney, S.A. (1991) *Ultramicroscopy*, 37, 79-89.
9. Popov, E.P. (1968) Introduction to the Mechanics of Solids, Prentice-Hall, Englewood Cliffs, NJ, 312.
10. Dieter, G.E. (1986) Mechanical Metallurgy, 3rd Edition, McGraw-Hill, New York, 88.
11. Carsley, J.E., Milligan, W.W., Hackney, S.A., and Aifantis, E.C. (1995) *Metall. Mater. Trans. A*, 26A, 2479-2481.
12. Carsley, J.E., Milligan, W.W., Hackney, S.A., and Aifantis, E.C. (1996) "Deformation Mechanisms in Bulk Fe - 10% Cu Nanostructures", in Processing and Properties of Nanocrystalline Materials, C. Suryanarayana, ed., TMS, Warrendale PA, in press.
13. Carsley, J.E., Ning, J., Milligan, W.W., Hackney, S.A., and Aifantis, E.C. (1995) *Nanostr. Mater.* 5, 441-448.
14. Hall, E.O. (1951) *Proc. Phys. Soc. B*, 64, 747.
15. Petch, N.J. (1953) *J. Iron Steel Inst.*, 174, 25.
16. Armstrong, R.W. (1983) in Yield, Flow and Fracture of Polycrystals, T.N. Baker, ed., Applied Science Publ., London, 1-31.
17. Aifantis, E.C. (1994) *J. Mech. Beh. Mater.*, 5, 355; and (1993) *Mat. Sci. Forum*, 123-125, 553.
18. Fougere, G.E., Weertman, J.R., Siegel, R.W., and Kim, S. (1992) *Scripta Metall.*, 26, 1879.
19. Nieman, G.W., Weertman, J.R., Siegel, R.W. (1991) *J. Mater. Res.*, 6, 1012.

20. Hackney, S.A., Ke, M., Milligan, W.W., and Aifantis, E.C. (1996) "Grain Size and Strain Rate Effects off Deformation and Fracture in Nanostructured Metals", in Processing and Properties of Nanocrystalline Materials, C. Suryanarayana, ed., TMS, Warrendale PA, in press.

21. Dieter, G.E. (1986) Mechanical Metallurgy, 3rd Edition, McGraw-Hill, New York, 455.

22. Hirth, J. P. and Lothe, J. (1982) Theory of Dislocations, Wiley, NY, 731-745.

23. Mukherjee, A. K., (1975) Grain Boundaries in Engineering Materials, Claitor Publishing, Baton Rouge, LA, 93.

24. Aifantis, E.C. (1992) *Int. J. Engr. Sci.*, 30, 1279-1299.

25. Barenblatt, G.I. (1962) *Adv. Appl. Mech.*, 7, 55-129.

26. Milligan, W.W., Hackney, S.A., and Aifantis, E.C. (1992) "Deformation and Damage at the Nanoscale: Preliminary Observations and Modeling", in ASME Symposium on Damage Mechanics and Localization, J.W. Ju and K.C. Valanis, eds., ASME, NY, MD vol. 34, 153-165.

27. Sherby, O.D. and Wadsworth, J. (1990) "Observations on historical and contemporary developments in superplasticity", in Superplasticity in Metals, Ceramics and Intermetallics, M.J. Mayo, M. Kobayashi and J. Wadsworth, eds., Materials Research Society, Pittsburgh, PA, 3-14.

28. Colios, J.A. and Aifantis, E.C. (1982) *Res. Mechanica*, 5, 67-85.

29. Chokshi, A.H. and Mukherjee, A.K. (1988) "Cavitation failure in superplastic alloys", in Superplasticity in Aerospace, H.C. Heikkenen and T.R. McNelley, eds., TMS, Warrendale PA, 167-182.

30. Milligan, W.W., Hackney, S.A., and Aifantis, E.C. (1995) "Constitutive Modeling for Nanostructured Materials", Chapter 11 in Continuum Models for Materials with Microstructure, H. Muhlhaus, Ed., Wiley, NY.

31. Aifantis, E.C. (1994) "Spatio-temporal instabilities in deformation and fracture", in Computational Material Modeling, AD-Vol. 42/PVP-Vol. 294, A.K. Noor and A. Needleman, Eds., ASME, New York, 199-222.

32. Romanov, A.E. and Aifantis, E.C. (1994) "Diffusion-like defect kinetics: Application to different plastic instabilities", in: Strength of Materials (JIMIC-2, ISCMA 10), H. Oikawa et al, Eds., Japan Institute of Metals, 307-310.

33. Romanov, A.E. and Aifantis, E.C. (1994) *Scripta Met. Mater.* 30, 1293-1398.

34. Romanov, A.E. and Aifantis, E.C. (1994) *Scripta Met. Mater.* 30, 1581-1586.

35. Zhu, H., Zbib, H.M., and Aifantis, E.C. (1995) *Acta Mechanica* 111, 111-124.

36. Unger, D.J. and Aifantis, E.C. (1995) *Int. J. Fracture*, 71, R27-R32.

37. Triantafyllidis, N. and Aifantis, E.C. (1986) *J. Elasticity*, 16, 225-238.

38. Ru, C.Q. and Aifantis, E.C. (1993) *Acta Mechanica*, 101, 59-68.

39. Webb, T.W. and Aifantis, E.C. (1995) *Int. J. Solids Struct.*, 32, 2725-2743.